

Heat Transfer Issues in Thin-Film Thermal Radiation Detectors

Mamadou Y. Barry

Thesis submitted to the faculty of the
Virginia Polytechnic Institute and State University
in partial fulfillment of the requirements for the degree of

**Master of Science
in
Mechanical Engineering**

Dr. J. R. Mahan, Chairman
Dr. Brian Vick
Dr. Thomas E. Diller

December 15, 1999
Blacksburg, VA

Keywords: heat conduction, thin-film, thermal radiation detector, composite materials,
and random walk.

Heat Transfer Issues in Thin-Film Thermal Radiation Detectors

Mamadou Y. Barry

J. Robert Mahan, Chairman

Mechanical Engineering

(ABSTRACT)

The Thermal Radiation Group at Virginia Polytechnic Institute and State University has been working closely with scientists and engineers at NASA's Langley Research Center to develop accurate analytical and numerical models suitable for designing next-generation thin-film thermal radiation detectors for earth radiation budget measurement applications. The current study provides an analytical model of the notional thermal radiation detector that takes into account thermal transport phenomena, such as the contact resistance between the layers of the detector, and is suitable for use in parameter estimation. It was found that the responsivity of the detector can increase significantly due to the presence of contact resistance between the layers of the detector. Also presented is the effect of doping the thermal impedance layer of the detector with conducting particles in order to electrically link the two junctions of the detector. It was found that the responsivity and the time response of the doped detector decrease significantly in this case. The corresponding decrease of the electrical resistance of the doped thermal impedance layer is not sufficient to significantly improve the electrical performance of the detector. Finally, the "roughness effect" is shown to be unable to explain the decrease in the thermal conductivity often reported for thin-film layers.

To my brother Toukara.

Acknowledgments

I would like to thank my advisor, Dr J. R. Mahan, for all his advice, support and kindness during my stay at Virginia Tech.

I would like to thank Dr. Brian Vick and Dr. Thomas E. Diller for serving on my advisory committee, and for their discussions and help.

I would like to thank NASA's Langley Research Center for supporting this research under NASA Grant # NAS-1-99128. A particular debt of gratitude is owed Mr. Edward H. Kist, Jr. in the Flight Electronics Systems Division.

I would like to thank all the members of the Thermal Radiation Group for their friendship and help.

I would like to thank Mme Nicole Jaffrin for motivating me to enroll at Virginia Tech and the *Université de Technologie de Compiègne* for allowing its students to have the opportunity to go overseas to pursue their studies.

I thank my family and especially my brother Alpha Boubacar for their support during my long studies abroad.

I thank also my wife Nathalie for her enormous support.

Merci beaucoup à vous tous.

Table of Contents

Chapter 1: Introduction.....	1
Chapter 2: The Effect Contact Resistance	6
2.1 Description of the notional thermal radiation detector	6
2.2 One-dimensional model of the detector with contact resistance	9
2.2.1 Steady-state temperature distribution.....	11
2.2.2 Transient temperature distribution.....	13
2.3 Results.....	24
Chapter 3: The Thin-Film Effect.....	29
3.1 Review of thin-film heat transfer.....	29
3.2 The thin-film thermal conductivity anomaly as a roughness effect	32
3.2.1 The random walk approach	33
3.2.1.1 Presentation of the technique	34
3.2.1.2 Results	38
3.2.2 Effective thermal conductivity of a thin-film layer of irregular thickness....	44
Chapter 4: Effect of Doping the Thermal Impedance Layer with Conducting Particles	48

4.1	Heat transfer in a heterogeneous material modeled as a coupled, two-step process.....	49
4.1.1	Formulation	49
4.1.2	Results	51
4.1.3	Discussion of the results.....	55
4.2	Heat transfer in a heterogeneous material using micromechanical property models.....	56
4.2.1	Thermal analysis	56
4.2.1.1	Effective thermal capacity of the mixture	57
4.2.1.2	Effective thermal conductivity.....	58
4.2.1.2.1	Dilute mixtures.....	58
4.2.1.2.2	Concentrated mixtures	59
4.2.1.3	Results	62
4.2.2	Electrical analysis	68
4.2.2.1	Effective properties	68
4.2.2.2	Results and Discussions.....	69
Chapter 5:	Conclusions and Recommendations	72
5.1	Conclusions	72
5.2	Recommendations.....	74
References	75
Appendix A:	homog.cpp	79
Appendix B:	randwalk2d.cpp.....	87
Appendix C:	eff_cond.cpp	91
Appendix D:	heterog.cpp	98
Vita	103

List of Illustrations

Figure 1: Configuration of the notional thermal radiation detector considered in this thesis.....	7
Figure 2: (a) Model of the detector with contact resistance, and (b) boundary conditions.....	10
Figure 3: Illustration of the superposition principle.....	14
Figure 4: Temperature response of the notional detector of Figure 1 with perfect thermal contact between all layers.	25
Figure 5: Temperature response of the notional detector of Figure 1 with a uniform thermal contact resistance between the layers.	26
Figure 6: Steady-state temperature response of the notional detector of Figure 1 for different values of interlayer contact conductance.....	26
Figure 7: Transient temperature response of the active junction of the notional thermal radiation of Figure 1 detector with no contact resistance (thermophysical properties given in Table 1).....	27
Figure 8: Time constant and responsivity of the notional detector of Figure 1 and Table 1 as a function of the thickness of the thermal impedance layer.....	28
Figure 9: The ratio of the longitudinal thin-film to the bulk conductivities as defined by Equations 3-3 and 3-4.....	32

Figure 10: Network of nodes for an arbitrary irregular geometry.	34
Figure 11: Flowchart of a two-dimensional random walk (continued on next page).	36
Figure 12: One-dimensional, steady-state heat transfer in a flat plate.	38
Figure 13: First two runs for $N = 50$ compared with exact temperature distribution for the problem defined by Figure 12.	40
Figure 14: First two runs for $N = 1000$ compared with the exact solution for the problem defined by Figure 12.	40
Figure 15: Comparison of the temperature distribution computed using the random walk method with $N = 5000$ and $n_y = 50$ with the exact solution for the problem defined by Figure 11 with.	42
Figure 16: Irregular geometry representing a layer of variable thickness.	43
Figure 17: Comparison of the temperature distribution computed using the random walk method at $x = 5 \mu\text{m}$ in Figure 16 with $n_y = 50$, $N = 1000$, 5000 , and 10000	43
Figure 18: Model of a hypothetical two-dimensional rough surface.	44
Figure 19: Control volume discretization of the hypothetical two-dimensional rough surface of Figure 18.	46
Figure 20: ratio of the effective thermal conductivity to the bulk thermal conductivity for the problem defined by Figures 18 and 19 with forty control volumes in the x direction and $L/H = 5$	46
Figure 21: Detector geometry with graphite doped thermal impedance layer.	49
Figure 22: Temperature response of the active junction with $h = 50 \text{ W/m}^2 \text{ K}$	52
Figure 23: Effect of contact conductance between the particles and the matrix on the steady-state temperature rise of the active junction.	53
Figure 24: Matrix and particle temperatures at $x = 12 \mu\text{m}$ for different values of the contact conductance.	54
Figure 25: Particle size effect on the steady-state temperature rise of the active junction for a volume fraction of particles of ten percent.	55

Figure 26: (a) lamina parallel to the heat flow direction; (b) lamina perpendicular to the heat flow direction. 61

Figure 27: Effective thermal conductivity of the doped thermal impedance layer for $K_d = k_m/k_d = 18.93$ and for a range of k_d/ah 63

Figure 28: Prediction of the effective thermal conductivity of the doped impedance layer for $k_m = 0.084$ W/m K and $k_d = 1.59$ W/m K..... 64

Figure 29: Active junction transient temperature rise of the detector with doped thermal impedance using homogeneous approximations method for a range of values of the volume fraction of the particles and $k_d/(ah) = 0$ 64

Figure 30: Active junction steady-state temperature rise and corresponding potential difference (Seebeck coefficient \times Temperature Rise) for a range of values of the volume fraction of the particles. 65

Figure 31: Temperature profile through the detector doped with fifty percent of carbon particles using the homogeneous approximations method to estimate the thermal conductivity and the heat capacity of the thermal impedance layer..... 67

Figure 32: Comparison of steady-state temperature profile through the detector obtained using (a) the two-step model, with (c) that obtained using the micromechanical model, and (b) the undoped detector model (the thermal impedance layer of the detector is doped with thirty percent of particles for the first two cases). 67

Figure 33: Thermal impedance layer doped with particles. 68

Figure 34: Effective resistivity of the thermal impedance layer defined by Figure 33 with $\sigma_m = 0.167 \times 10^{-14} \Omega^{-1} m^{-1}$ 71

Figure 35: Effective electrical resistance of the thermal impedance layer defined by Figure 33 with $L = 25.4 \mu m$ and $S = 60 \times 60 \mu m^2$ 71

List of Tables

Table 1: Thermophysical properties of materials used in the baseline thermal radiation detector model [Weckmann, 1997].	8
Table 2: Error values for different runs of the random walk solution to the problem defined by Figure 11 with $n_y = 50$	39
Table 3: Influence of the number of random walks on the machine time and the mean error for the problem defined by Figure 12 with $n_y = 50$	41

Nomenclature

Symbols:

a	diameter of the particles, μm	h_c	uniform contact resistance between the layers of the detector, $\text{W}/\text{m}^2 \text{K}$
$A_{i,m}, B_{i,m}$	coefficients in $X_{i,m}$	$h_{i,j+1}$	$i = 1$ to 5. contact resistance between the layers i and $i+1$, $\text{W}/\text{m}^2 \cdot \text{K}$
A_p	surface area of a particle, m^2	$H_{i,j+1}$	$k_i / (h_{i,j+1} \sqrt{\alpha_i})$
C	phonon specific heat, $\text{J}/\text{m}^3 \text{K}$	k_i	$i = 1$ to 6. thermal conductivity of the layer i , $\text{W}/\text{m K}$
C_m	<ul style="list-style-type: none"> coefficients in $\theta_{i,j}$ (Chapter 1) heat capacity of the matrix per total volume, $(1-f)(\rho c)_m$ (Chapter 4) 	$K_{i,j+1}$	$k_i / k_{i+1} \sqrt{\alpha_{i+1} / \alpha_i}$
C_p	heat capacity of the particles per total volume, $f(\rho c)_p$	K	$(1-f)k_m$
f	volume fraction of the particles	\bar{k}	effective thermal conductivity, $\text{W}/\text{m K}$
f_i'	mass fraction of i	\bar{K}	relative effective thermal conductivity, \bar{k} / k_m
f_i	volume fraction of i .	K_d	k_d / k_m
H	<ul style="list-style-type: none"> coupling coefficient (Chapter 4) thickness, m (Chapter 3) 	k	thermal conductivity, $\text{W}/\text{m K}$
h	contact conductance between the particles and the matrix, $\text{W}/\text{m}^2 \text{K}$	l	phonon mean free path, m

M_i^j	$i, j = 1 \text{ to } 11$. element of the line i and the column j of the matrix in Equation 2-47	t	physical time, s
N	<ul style="list-style-type: none"> • number of random walks (Chapter 2) • number of particles per volume (Chapter 4) 	$T_{m,j}^i$	matrix temperature at the node j and time step i , K
N_m	normalization integral	$T_{p,j}^i$	particle temperature at the node j and time step i , K
n_y	number of nodes in the y direction	v	speed of sound, m
n_r	number of runs	V	volume, m^3
q	heat flux, W/m^2	T_{rw}	temperature computed using the random walk method, K
Q_i	heat flux through the element i , W/m	$\langle T_{rw} \rangle$	random walk temperature mean, K
Q_T	total heat flux, W/m	x, y	cartesian coordinates, m
r	random number	x_i	$i = 1 \text{ to } 6$. coordinate of the upper surface of the layer i , m
R	amplitude of the roughness, m	$X_{i,m}$	$i = 1 \text{ to } 6$. space-dependant function corresponding to the m th eigenvalue
\bar{R}	effective electrical resistance, Ω		

Greek Symbols:

α_i	$i = 1 \text{ to } 6$. thermal diffusivity of the layer i , m^2/s	ε	error
β_m	m th eigenvalue	$\langle \varepsilon \rangle$	mean error
δ	ratio of the film thickness to the mean free path	$\bar{\varphi}$	effective resistivity, $\Omega \text{ m}$
Δx	step size in the x direction, m	$\bar{\Lambda}$	relative effective electrical conductivity, $\bar{\sigma}/\sigma_m$
Δy	step size in the y direction, m		

Λ_d	σ_d/σ_m	$\overline{\rho c}$	effective heat capacity of the matrix-particle mixture, J/m ³ K
μ	micro		
θ_i	$i = 1$ to 6 . transient temperature rise above the substrate temperature of the layer i , K	σ	electrical conductivity, $\Omega^{-1} \text{ m}^{-1}$
$\theta_{s,i}$	$i = 1$ to 6 . steady-state component of θ_i , K	$\overline{\sigma}$	effective electrical conductivity, $\Omega^{-1} \text{ m}^{-1}$
$\theta_{t,i}$	$i = 1$ to 6 . transient component of θ_i , K	ζ_0	counter

Subscripts:

p	particle property (Section 4-1)
m	matrix property
d	particles property (Section 4-2)
eff	effective property
bulk	bulk property
mixture	mixture property

Chapter 1: Introduction

For many years the Thermal Radiation Group (TRG) at Virginia Polytechnic Institute and State University, under the direction of Professor J.R. Mahan, has been involved in developing advanced numerical tools for modeling the optical, thermal and electrical processes in thermal radiation detectors. During the last two years the Group, working with scientists and engineers at NASA's Langley Research Center, has pursued the design of a new thermal radiation detector to be used for more accurate measurements of the earth radiation budget (ERB) from space. The ERB refers to the balance at the top of the atmosphere between the incoming energy from the sun and the outgoing thermal and reflected energy from the earth.

The growing interest in ground-based measurements using instruments such as pyranometers [Smith, 1999], which are cheaper and easier to monitor than space-borne instruments, makes it crucial for the proponents of space-borne measurements to develop more reliable instruments using the latest technologies available in order to remain competitive. The sensors of these latter instruments have to be as small as possible, with extremely short time response and a maximum responsivity, so that they can be organized into linear or focal-plane arrays [Weckmann, 1997; Barreto, 1998; Sanchez, 1998; Sorensen, 1998]. These factors all favor the development of a thin-film multilayer thermal radiation detector technology, as illustrated in Figure 1. In this approach six layers of material are sputtered onto a substrate to form the detector. This allows layers on the order of a few microns thick. The absorption of thermal radiation by the absorber layer increases the temperature of the active junction, and the difference of temperature

between this active junction and the reference junction generates an electromotive force proportional to the temperature difference between them.

Analysis of heat transfer in the resulting thin-film thermal radiation detector is essential for its successful design and for the prediction of its performance. Creation of the heat transfer model requires applying either macroscale or microscale transport theories, depending on the physical dimensions (length scales) of the detector and its frequency response characteristics (time scale). If macroscale heat transfer theory is applied to a microscale problem in a situation for which it is inappropriate, then a significant error in the calculated heat transfer rate or temperature distribution can result [Flik et al., 1992]. The model also requires the precise knowledge of the thermophysical properties of materials used in the conception of the detector. With the contemplated geometry and fabrication technique, several interesting questions arise, and the performance of the detector will depend on the response to these questions. Ignoring these nuances could lead to very poor thermal models of the detector.

Normally the thermal resistance offered to heat conduction by a uniform layer is directly proportional to its thickness. When two materials having different thermal conductivities are in mechanical contact, a temperature discontinuity can occur at their interface. This temperature jump results from *contact resistance* between the two layers. In fact, even with thin-films, perfect contact at the interface occurs only at a limited number of spots [Hmina et al., 1997; Kelkar et al., 1996] and the void found elsewhere between the layers is filled with gas or a vacuum. It is possible that the intrinsic thermal resistance of a thin film is significantly smaller than the contact resistance at the interface. Modeling the detector without taking into account this hypothetical contact resistance could lead to a serious departure from reality. Even if the values of the contact resistances between the different layers are not currently known, it is important to include them in the thermal models. These more general models can then be used by other members of the Thermal Radiation Group who are developing parameter estimation techniques aimed at recovering the thermophysical properties of the detector. The use of fictitious contact resistance values in the model will reveal the importance of that factor to the performance of the detector.

The correct treatment of the *thin-film effect* is another key factor in the process of obtaining a good thermal model. The thin-film effect has been defined in terms of the departure of the thermal conductivity of a layer from its bulk value as the thickness of the layer approaches the order of magnitude of the mean free path of the energy carriers, a definition that presupposes that Fourier's law of heat conduction governs thin-film heat transfer. However the thin-film effect implies the use of microscale heat transfer theories. In these theories the classical Fourier's law no longer describes the temperature and heat flow fields, and the thermal conductivity loses its meaning as an intrinsic thermal property of the thin-film material. Several analytical [Flik et al., 1990; and Kumar et al., 1994] and experimental [Nath et al., 1974; Lambropoulos et al., 1989; Lee et al., 1997; and Orain et al., 1998] studies have shown that the thermal conductivity of thin-film layers, defined as the heat flux divided by the temperature difference across the layer per unit thickness, can be several orders of magnitude lower than that of the bulk material. The closed-form models for computing thermal transport in such cases require the knowledge of material properties such as the mean free path that are unknown for materials contemplated for use in the notional detector.

In the current effort the use of a geometrical property characterizing the *mechanical roughness* of the film layer is considered in an attempt to show the dependence between the effective thermal conductivity and the layer thickness. It is evident that in a thin film, the roughness of the layer can be of the same order of magnitude as the layer thickness itself. The idea here is to try to explain the decrease of the thermal conductivity often attributed to the thin-film effect in terms of a roughness effect. A numerical thermal model derived from a macroscale approach with the roughness as a parameter is used to analyze the dependence of the effective thermal conductivity on the roughness of the layer.

The overall distance between the two thermocouple junctions of the notional detector shown in Figure 1 is less than fifty microns. Another problem that arises is how to electrically connect these two junctions. Fabrication and size limitations preclude the use of a traditional electrical conductor (a "wire" lead) to connect these two junctions. The NASA design team led by Kist [1999] has proposed that the thermal impedance layer

between the two thermocouple junctions also double as an electrical conductor. One idea would be to dope the thermal impedance layer with carbon particles. It is hoped that these particles would then effect the electrical connection between the junctions without completely eliminating the thermal impedance needed to maintain the temperature difference between the active and reference thermocouple junctions. Two different approaches are considered in order to characterize the thermal and electrical behavior of this new detector configuration. The first approach consists of using a model adapted from Vick and Scott [1998]. The second approach models the heterogeneous thermal impedance layer of the detector using micromechanical approximations to obtain averaged electrical and thermophysical properties. In the first approach the thermal impedance layer is modeled as a matrix with embedded small particles, and heat is assumed to be transferred from the matrix to the separated particles. The temperature distribution within such a layer is obtained by solving two coupled equations derived from the energy balance of the matrix and the particles. In the second approach, an equivalent thermal conductivity and heat capacity are used to represent an appropriately layered medium, and the detector is modeled as if the layers were homogeneous. The same homogeneous approximations are also used in order to analyze the change of the electrical resistance of the doped thermal impedance layer. In either case, the resulting model would need to be suitable for later use in a parameter estimation scheme.

Objectives

The objectives of the current investigation are to explore the following three questions:

- How might the presence of contact resistance influence the response of the detector?
- Can the so-called thin-film effect be explained and treated as a roughness effect?
- What is the effect of the addition of electrically conducting particles in the thermal impedance layer on the performance of the detector?

Even if the answer to the second question is negative, a secondary goal is to advance the Group's knowledge of this interesting phenomenon.

In pursuing the answers of these questions the author has profited from the fruits of earlier investigations by members of the Thermal Radiation Group. Weckmann's [1997] model of the dynamic electrothermal response of a similar thermal radiation detector ignored contact resistance and did not speculate on the possible consequences of a "thin-film" effect. Sánchez [1998] formulated a Monte-Carlo ray-trace radiative model of an integrated detector concept in which a linear array of the detectors from Weckmann's thesis was bonded to the wall of a V-groove cavity, and Barreto [1998] designed experiments for estimating the electro-thermophysical properties of the materials in Weckmann's detector concept. More recently Sorensen [1998] performed analytical and experimental characterizations of some aspects of the detector. Sorensen is currently developing genetic and hybrid algorithms and designing experiments to estimate the electro-thermophysical properties of detectors such as the one shown in Figure 1.

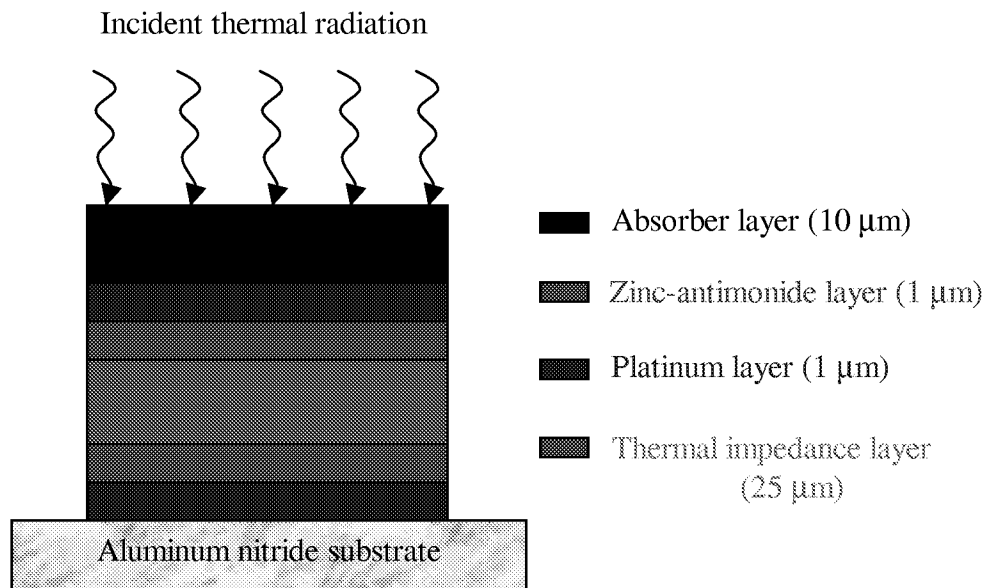
Chapter 2 addresses the problem of modeling the effects of contact resistance for use in the optimal design of experiments aimed at recovering its value.

Chapter 2: The Effect Contact Resistance

Three questions bearing on the electrothermal performance of thin-film thermal radiation detectors were posed in Chapter 1. In the current chapter, one of these questions, that concerning contact resistance, is explored in detail.

2.1 Description of the notional thermal radiation detector

The notional thermal radiation detector considered in this thesis consists of six parallel layers of different materials, as illustrated in Figure 1. A 1.0- μm thick platinum layer is deposited on an aluminum-nitride substrate, and then a 1.0- μm zinc-antimonide layer is sputtered over the platinum. Next, a 25- μm thick thermal impedance layer is deposited over the zinc-antimonide layer. Then additional layers of zinc-antimonide and platinum are deposited on the thermal impedance layer. Finally, the platinum is coated with a 10- μm thick black absorber layer to increase the absorption of thermal radiation. The platinum/zinc-antimonide layer near the substrate forms the reference junction of the thermocouple, and the platinum/zinc-antimonide layer on the thermal impedance layer forms the active junction. The junction materials are chosen to provide the highest available Seebeck coefficient [Weckmann, 1997]. In this baseline configuration the thermal impedance is not doped with carbon particles. The doped configuration is considered in Chapter 4. The thermal impedance layer considered in the current chapter is assumed to be fabricated from Parylene. The nominal properties of the material used in the detector are given in Table 1.



[Not to scale]

Figure 1: Configuration of the notional thermal radiation detector considered in this thesis.

Table 1: Thermophysical properties of materials used in the baseline thermal radiation detector model [Weckmann, 1997].

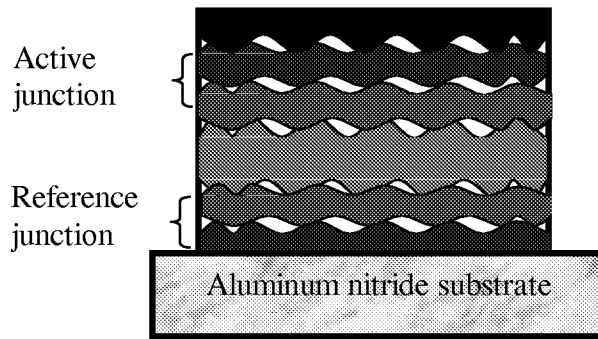
	Mass density (kg/m ³)	Specific heat (J/kg·K)	Conductivity (W/m·K)	Diffusivity (m ² /s)	Seebeck Coefficient (V/K)
Aluminum Substrate	3260	800	165	6.33×10 ⁻⁵	N/A
Absorber Layer	1400	669	0.209	2.23×10 ⁻⁷	N/A
Parylene	1289	712	0.084	9.15×10 ⁻⁸	N/A
Platinum	21450	133	71.6	2.51×10 ⁻⁵	N/A
Zinc Antimonide	6880	200	60	4.4×10 ⁻⁵	N/A
Carbon	2620	710	1.59	8.55×10 ⁻⁷	N/A
Platinum/Zinc-Antimonide Junction	N/A	N/A	65.3	3.09×10 ⁻⁵	960×10 ⁻⁶

2.2 One-dimensional model of the detector with contact resistance

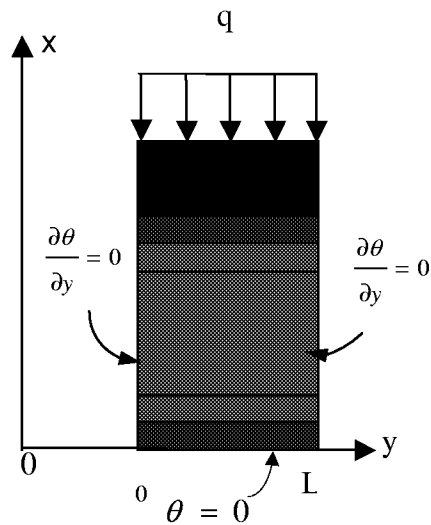
Due to the thickness of the layers of the thermal detector, on the order of a few microns, the thermal resistance resulting from the imperfect contact between layers, illustrated in Figure 2(a), may play an important role in the overall thermal resistance. In fact, a careful search of the literature provided no insight into the nature of the interface and the consequent contact resistance at the interface between the sputtered materials in the notional detector. With contact resistance, the temperature profile through the detector would be discontinuous at the interfaces between layers. The first objective of the model is to validate the results obtained assuming perfect thermal contact. A preliminary study is also carried out to evaluate the effect of the thickness of a Parylene thermal impedance layer on detector time response and responsivity.

In order to develop a one-dimensional analytical model we assume for both the steady-state and transient cases that:

- the thermophysical properties (conductivity, specific heat, density) are constant and uniform,
- thermal radiation is negligible,
- Fourier's law is valid, and
- internal heat generation is absent.



(a)



(b)

[Not to scale]

- | | | |
|------------------|---------------------------|--------|
| ■ Absorber layer | ■ Zinc-Antinomide layer | □ void |
| ■ Platinum layer | ■ Thermal impedance layer | |

Figure 2: (a) Model of the detector with contact resistance, and (b) boundary conditions.

2.2.1 Steady-state temperature distribution

For each layer (i) the steady-state temperature rise $\theta_{s,j}(x)$ above the substrate temperature is governed by

$$\frac{d^2\theta_{s,i}}{dx^2} = 0 \quad , \quad x_i < x < x_{i+1}, \quad i = 1,2,\dots,6, \quad (2-1)$$

subject to the boundary conditions, indicated in Figure 2(b),

$$\theta_{s,1} = 0 \quad , \quad \text{at} \quad x = 0 \quad , \quad (2-2)$$

$$\left\{ \begin{array}{l} -k_i \frac{d\theta_{s,i}}{dx} = h_{i,i+1} (\theta_{s,i} - \theta_{s,i+1}) \quad , \quad \text{at the interfaces } x = x_{i+1}, \\ k_i \frac{d\theta_{s,i}}{dx} = k_{i+1} \frac{d\theta_{s,i+1}}{dx} \quad , \quad i = 1,2,\dots,5, \end{array} \right. \quad (2-3)$$

$$\text{and} \quad k_6 \frac{d\theta_{s,6}}{dx} = q \quad , \quad \text{at} \quad x = x_6 \quad . \quad (2-5)$$

The heat flux q is uniform through the different layers.

The differential equations given by Equations 2-1 through 2-5 can be solved directly.

For the first layer

$$\frac{d^2\theta_{s,1}}{dx^2} = 0 \quad , \quad (2-6)$$

$$\theta_{s,1} = 0 \quad , \quad \text{at} \quad x = 0 \quad , \quad (2-7)$$

$$\text{and} \quad q = k_1 \frac{d\theta_{s,1}}{dx} \quad , \quad \text{at} \quad x = x_1 \quad . \quad (2-8)$$

The temperature profile is then $\theta_{s,1}(x) = \frac{q}{k_1}x$. (2-9)

For the second layer

$$\frac{d^2\theta_{s,2}}{dx^2} = 0 \quad , \quad (2-10)$$

$$-k_1 \frac{d\theta_{s,1}}{dx} = h_{1,2} [\theta_{s,1}(x_1) - \theta_{s,2}(x_1)] \quad \text{at} \quad x = x_1 \quad , \quad (2-11)$$

and $q = k_2 \frac{d\theta_{s,2}}{dx}$ at $x = x_2$. (2-12)

Thus, $\theta_{s,2}(x) = q \left[\frac{x}{k_2} + x_1 * \left(\frac{1}{k_1} - \frac{1}{k_2} \right) + \frac{1}{h_{12}} \right]$. (2-13)

More generally the steady-state temperature distribution for any layer is given by

$\theta_{s,1} = \frac{q}{k_1}x$
and (2-14)

$$\theta_{s,i} = q \left(\frac{x}{k_i} + \sum_{j=2}^{i-1} x_{j-1} \left(\frac{1}{k_{j-1}} - \frac{1}{k_j} \right) + \sum_{m=1}^{i-1} \frac{1}{h_{m,m+1}} \right), \quad i \geq 2.$$

2.2.2 Transient temperature distribution

The differential equation describing the evolution of the transient temperature rise $\theta_i(x,t)$ above the substrate temperature for each layer is

$$\frac{\partial^2 \theta_i(x,t)}{\partial x^2} = \frac{1}{\alpha_i} \frac{\partial \theta_i(x,t)}{\partial t} \quad \text{in} \quad x_i < x < x_{i+1}, \quad t > 0, \quad (2-15)$$

where $i = 1, 2, \dots, 6$, subject to the boundary conditions

$$\theta_1(0,t) = 0 \quad \text{at} \quad x = x_1, \quad (2-16)$$

$$\left\{ \begin{array}{l} -k_i \frac{\partial \theta_i}{\partial x} = h_{i,i+1} (\theta_i - \theta_{i+1}) \\ k_i \frac{\partial \theta_i}{\partial x} = k_{i+1} \frac{\partial \theta_{i+1}}{\partial x} \end{array} \right. \quad \text{at the interfaces} \quad x = x_{i+1}, \quad (2-17)$$

$$, \quad i = 1, 2, \dots, 5, \quad t > 0, \quad (2-18)$$

and

$$k_6 \frac{\partial \theta_6}{\partial x} = q \quad \text{at} \quad x = x_6, \quad t > 0. \quad (2-19)$$

$$\text{The initial condition is} \quad \theta_i(x,0) = 0. \quad (2-20)$$

This problem can be solved by different techniques, including the finite difference method, by the finite element method and by finite integral transforms. However an analytical solution being more convenient for later parameter estimation studies, the orthogonal expansion technique [Özsisik, 1993] for a multi-layer medium with perfect contact between layers is adapted to the transient model described by Equations 2-15 through 2-20. The problem involves a nonhomogeneous boundary condition at $x = x_6$ (at the top of the detector) and so cannot be directly solved using separation of variables. In order to transform this nonhomogeneous boundary condition into a homogeneous one, we

consider that $\theta_i(x,t)$ is obtained by the superposition of two problems, as suggested in Figure 3:

- a steady-state problem with specified heat flux at $x = x_6$: $\theta_{s,i}(x)$
- a transient problem with insulated boundary at $x = x_6$: $\theta_{t,i}(x,t)$

Thus
$$\theta_i(x,t) = \theta_{s,i}(x) + \theta_{t,i}(x,t) . \tag{2-21}$$

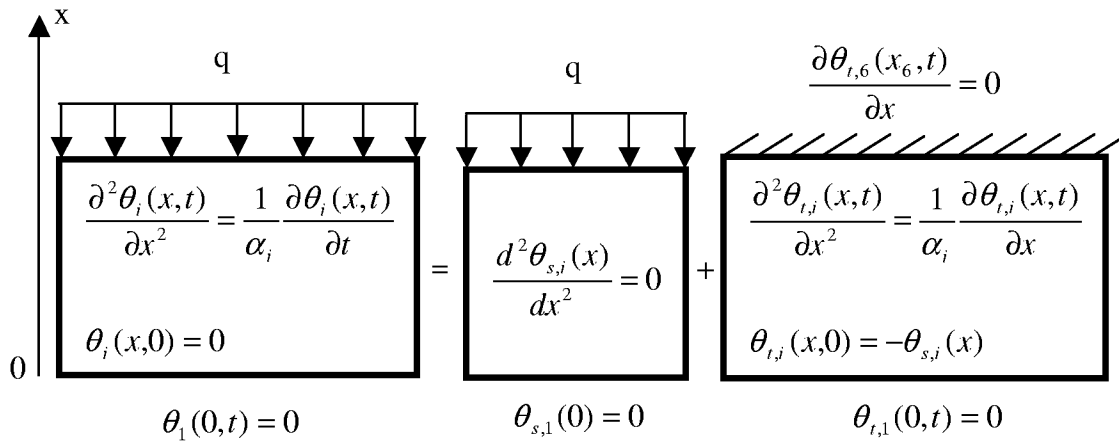


Figure 3: Illustration of the superposition principle.

The steady-state problem is described by an ordinary differential equation and has already been solved; the solution is given by Equation 2-14.

The transient solution $\theta_{t,i}(x,t)$ is governed by a homogeneous partial differential equation and is solved using the separation of variables technique. Let us assume that $\theta_{t,i}(x,t)$ may be expressed

$$\theta_{t,i}(x,t) = X_i(x)\Gamma(t) . \tag{2-22}$$

Substitution into Equation 2-15 yields

$$\frac{\partial^2 (X_i(x)\Gamma(t))}{\partial x^2} = \frac{1}{\alpha_i} \frac{\partial (X_i(x)\Gamma(t))}{\partial t} \quad . \quad (2-23)$$

Thus

$$\frac{\alpha_i}{X_i} \frac{d^2 X_i}{dx^2} = \frac{1}{\Gamma} \frac{d\Gamma}{dt} = -\beta^2 \quad , \quad (2-24)$$

where the eigenvalue β is the separation constant. The minus sign in front of β^2 is required to capture the exponential nature of the variation with time. The change of variables transforms the partial differential equation into two ordinary differential equations,

$$\frac{d\Gamma_m}{dt} + \beta_m^2 \Gamma_m = 0 \quad (2-25)$$

and

$$\frac{d^2 X_{i,m}}{dx^2} + \frac{\beta_m^2}{\alpha_i} X_{i,m} = 0 \quad . \quad (2-26)$$

The subscript m is used in Equations 2-25 and 2-26 to indicate that there are an infinite number of eigenvalues β_m .

For a given eigenvalue the solution of Equation 2-25 is obtained directly as

$$\Gamma_m(t) = e^{-\beta_m^2 t} \quad . \quad (2-27)$$

The complete solution is then of the form

$$\theta_{i,i}(x,t) = \sum_{m=1}^{\infty} C_m X_{i,m}(x) e^{-\beta_m^2 t}, \quad (2-28)$$

where the coefficients C_m are eventually obtained by exploiting the orthogonality property.

The ordinary differential equation to be solved to obtain the eigenfunctions $X_{i,m}$ and the corresponding eigenvalues is

$$\frac{d^2 X_{i,m}}{dx^2} + \frac{\beta_m^2}{\alpha_i} X_{i,m} = 0, \quad x_i < x < x_{i+1}, \quad i = 1, \dots, 6, \quad (2-29)$$

with boundary conditions

$$X_{1m}(0) = 0 \quad \text{at} \quad x = 0, \quad (2-30)$$

$$\left\{ \begin{array}{l} k_i \frac{dX_{i,m}}{dx} = k_{i+1} \frac{dX_{i+1,m}}{dx} \\ -k_i \frac{dX_{i,m}}{dx} = h_{i,i+1} (X_{i,m} - X_{i+1,m}), \quad i = 1, 2, \dots, 5 \end{array} \right. \quad \text{at the interfaces} \quad x = x_i, \quad (2-31)$$

$$\left\{ \begin{array}{l} k_i \frac{dX_{i,m}}{dx} = k_{i+1} \frac{dX_{i+1,m}}{dx} \\ -k_i \frac{dX_{i,m}}{dx} = h_{i,i+1} (X_{i,m} - X_{i+1,m}), \quad i = 1, 2, \dots, 5 \end{array} \right. \quad (2-32)$$

and $k_6 \frac{dX_{6m}}{dx} = 0 \quad \text{at} \quad x = x_6. \quad (2-33)$

The general solution of this eigenvalue problem is [Özsisik, 1993]

$$X_{i,m}(x) = A_{i,m} \sin\left(\frac{\beta_m}{\sqrt{\alpha_i}} x\right) + B_{i,m} \cos\left(\frac{\beta_m}{\sqrt{\alpha_i}} x\right). \quad (2-34)$$

Let us assume that $\eta_i = \frac{\beta_m}{\sqrt{\alpha_i}} x_i$. (2-35)

Then Equation 2-34 becomes

$$X_{i,m}(x) = A_{i,m} \sin\left(\eta_i \frac{x}{x_i}\right) + B_{i,m} \cos\left(\eta_i \frac{x}{x_i}\right) . \quad (2-36)$$

The derivative of Equation 2-36 is

$$\frac{dX_{i,m}}{dx} = \frac{\beta_m}{\sqrt{\alpha_i}} \left[A_{i,m} \cos\left(\eta_i \frac{x}{x_i}\right) - B_{i,m} \sin\left(\eta_i \frac{x}{x_i}\right) \right] . \quad (2-37)$$

Substitution of Equations 2-35 and 2-37 into Equations 2-31 and 2-32 yields

$$A_{i+1,m} \sin\left(\frac{x_i}{x_{i+1}} \eta_{i+1}\right) + B_{i+1,m} \cos\left(\frac{x_i}{x_{i+1}} \eta_{i+1}\right) \quad (2-38)$$

$$= A_{i,m} [\sin(\eta_i) + \beta_m H_{i,j+1} \cos(\eta_i)] + B_{i,m} [\cos(\eta_i) - \beta_m H_{i,j+1} \sin(\eta_i)]$$

and

$$A_{i+1,m} \cos\left(\frac{x_i}{x_{i+1}} \eta_{i+1}\right) - B_{i+1,m} \sin\left(\frac{x_i}{x_{i+1}} \eta_{i+1}\right) = K_{i,j+1} [A_{i,m} \cos(\eta_i) - B_{i,m} \sin(\eta_i)] , \quad (2-39)$$

where
$$H_{i,i+1} = \frac{k_i}{h_{i,j+1} \sqrt{\alpha_i}} \quad (2-40)$$

and
$$K_{i,i+1} = \frac{k_i}{k_{i+1}} \sqrt{\frac{\alpha_{i+1}}{\alpha_i}}. \quad (2-41)$$

In matrix form Equations 2-38 and 2-39 can be written

$$\begin{bmatrix} \sin(x_i \eta_{i+1} / x_{i+1}) & \cos(x_i \eta_{i+1} / x_{i+1}) \\ \cos(x_i \eta_{i+1} / x_{i+1}) & -\sin(x_i \eta_{i+1} / x_{i+1}) \end{bmatrix} \begin{bmatrix} A_{i+1,m} \\ B_{i+1,m} \end{bmatrix} \quad (2-42)$$

$$= \begin{bmatrix} \sin(\eta_i) + H_{i,i+1} \beta_m \cos(\eta_i) & \cos(\eta_i) - H_{i,i+1} \beta_m \sin(\eta_i) \\ K_{i,i+1} \cos(\eta_i) & -K_{i,i+1} \sin(\eta_i) \end{bmatrix} \begin{bmatrix} A_{i,m} \\ B_{i,m} \end{bmatrix}.$$

Solving Equation 2-42 for the unknown coefficients $A_{i,m}$ and $B_{i,m}$ yields

$$A_{i+1,m} = U_{i,m} \sin\left(\frac{x_i}{x_{i+1}} \eta_{i+1}\right) + V_{i,m} \cos\left(\frac{x_i}{x_{i+1}} \eta_{i+1}\right), \quad i = 1, 2, \dots, 5, \quad (2-43)$$

and

$$B_{i+1,m} = U_{i,m} \cos\left(\frac{x_i}{x_{i+1}} \eta_{i+1}\right) - V_{i,m} \sin\left(\frac{x_i}{x_{i+1}} \eta_{i+1}\right), \quad i = 1, 2, \dots, 5, \quad (2-44)$$

where

$$U_{i,m} = A_{i,m} [\sin(\eta_i) + \beta_m H_{i,i+1} \cos(\eta_i)] + B_{i,m} [\cos(\eta_i) - H_{i,i+1} \beta_m \sin(\eta_i)] \quad (2-45)$$

and

$$V_{i,m} = K_{i,i+1} [A_{i,m} \cos(\eta_i) - B_{i,m} \sin(\eta_i)] \quad . \quad (2-46)$$

The boundary condition given by Equation 2-30 requires that $B_{1,m} = 0$. Thus we can set

$$A_{1,m} = 1.$$

All of the coefficients $A_{i,m}$ and $B_{i,m}$ can now be computed using Equations 2-43 and 2-44. Introducing $A_{1,m} = 1$ into Equation 2-42 and expanding it for the six layers of the detector yields

$$\begin{bmatrix} M_1^1 & M_1^2 & M_1^3 & 0 & 0 & 0 & 0 & 0 & 0 & 0 & 0 & 0 \\ M_2^1 & M_2^2 & M_2^3 & 0 & 0 & 0 & 0 & 0 & 0 & 0 & 0 & 0 \\ 0 & M_3^2 & M_3^3 & M_3^4 & M_3^5 & 0 & 0 & 0 & 0 & 0 & 0 & 0 \\ 0 & M_4^2 & M_4^3 & M_4^4 & M_4^5 & 0 & 0 & 0 & 0 & 0 & 0 & 0 \\ 0 & 0 & 0 & M_5^4 & M_5^5 & M_5^6 & M_5^7 & 0 & 0 & 0 & 0 & 0 \\ 0 & 0 & 0 & M_6^4 & M_6^5 & M_6^6 & M_6^7 & 0 & 0 & 0 & 0 & 0 \\ 0 & 0 & 0 & 0 & 0 & M_7^6 & M_7^7 & M_7^8 & M_7^9 & 0 & 0 & 0 \\ 0 & 0 & 0 & 0 & 0 & M_8^6 & M_8^7 & M_8^8 & M_8^9 & 0 & 0 & 0 \\ 0 & 0 & 0 & 0 & 0 & 0 & 0 & M_9^8 & M_9^9 & M_9^{10} & M_9^{11} & 0 \\ 0 & 0 & 0 & 0 & 0 & 0 & 0 & M_{10}^8 & M_{10}^9 & M_{10}^{10} & M_{10}^{11} & 0 \\ 0 & 0 & 0 & 0 & 0 & 0 & 0 & M_{11}^8 & M_{11}^9 & M_{11}^{10} & M_{11}^{11} & 0 \end{bmatrix} \begin{bmatrix} 1 \\ A_{2m} \\ B_{2m} \\ A_{3m} \\ B_{3m} \\ A_{4m} \\ B_{4m} \\ A_{5m} \\ B_{5m} \\ A_{6m} \\ B_{6m} \end{bmatrix} = \begin{bmatrix} 0 \\ 0 \\ 0 \\ 0 \\ 0 \\ 0 \\ 0 \\ 0 \\ 0 \\ 0 \\ 0 \end{bmatrix}, \quad (2-47)$$

where

$$M_1^1 = \sin \eta_1 + H_{1,2} \cos \eta_1 \quad ,$$

$$M_1^2 = -\sin \left(\frac{x_1}{x_2} \eta_2 \right) \quad ,$$

$$M_1^3 = -\cos \left(\frac{x_1}{x_2} \eta_2 \right) \quad ,$$

$$M_2^1 = K_{1,2} \cos \eta_1 \quad ,$$

$$M_2^2 = -\cos\left(\frac{x_1}{x_2} \eta_2\right) \quad ,$$

$$M_2^3 = \sin\left(\frac{x_1}{x_2} \eta_2\right) \quad ,$$

$$M_3^2 = \sin \eta_2 + H_{2,3} \cos \eta_2 \quad ,$$

$$M_3^3 = \cos \eta_2 - H_{2,3} \sin \eta_2 \quad ,$$

$$M_3^4 = -\sin\left(\frac{x_2}{x_3} \eta_3\right) \quad ,$$

$$M_3^5 = -\cos\left(\frac{x_2}{x_3} \eta_3\right) \quad ,$$

$$M_4^2 = K_{2,3} \cos \eta_2 \quad ,$$

$$M_4^3 = -K_{2,3} \sin \eta_2 \quad ,$$

$$M_4^4 = -\cos\left(\frac{x_2}{x_3} \eta_3\right) \quad ,$$

$$M_4^5 = \sin\left(\frac{x_2}{x_3} \eta_3\right) \quad ,$$

$$M_5^4 = \sin \eta_3 + H_{3,4} \cos \eta_3 \quad ,$$

$$M_5^5 = \cos \eta_3 - H_{3,4} \sin \eta_3 \quad ,$$

$$M_5^6 = -\sin\left(\frac{x_3}{x_4}\eta_4\right) ,$$

$$M_5^7 = -\cos\left(\frac{x_3}{x_4}\eta_4\right) ,$$

$$M_6^4 = K_{3,4} \cos\eta_3 ,$$

$$M_6^5 = -K_{3,4} \sin\eta_3 ,$$

$$M_6^6 = -\cos\left(\frac{x_3}{x_4}\eta_4\right) ,$$

$$M_6^7 = \sin\left(\frac{x_3}{x_4}\eta_4\right) ,$$

$$M_7^6 = \sin\eta_4 + H_{4,5} \cos\eta_4 ,$$

$$M_7^7 = \cos\eta_4 - H_{4,5} \sin\eta_4 ,$$

$$M_7^8 = -\sin\left(\frac{x_4}{x_5}\eta_5\right) ,$$

$$M_7^9 = -\cos\left(\frac{x_4}{x_5}\eta_5\right) ,$$

$$M_8^6 = K_{4,5} \cos\eta_4 ,$$

$$M_8^7 = -K_{4,5} \sin\eta_4 ,$$

$$M_8^8 = -\cos\left(\frac{x_4}{x_5}\eta_5\right) ,$$

$$M_8^9 = \sin\left(\frac{x_4}{x_5}\eta_5\right) \quad ,$$

$$M_9^8 = \sin\eta_5 + H_{5,6} \cos\eta_5 \quad ,$$

$$M_9^9 = \cos\eta_5 - H_{5,6} \sin\eta_5 \quad ,$$

$$M_9^{10} = -\sin\left(\frac{x_5}{x_6}\eta_6\right) \quad ,$$

$$M_9^{11} = -\cos\left(\frac{x_5}{x_6}\eta_6\right) \quad ,$$

$$M_{10}^8 = K_{5,6} \cos\eta_5 \quad ,$$

$$M_{10}^9 = -K_{5,6} \sin\eta_5 \quad ,$$

$$M_{10}^{10} = -\cos\left(\frac{x_5}{x_6}\eta_6\right) \quad ,$$

$$M_{10}^{11} = \sin\left(\frac{x_5}{x_6}\eta_6\right) \quad ,$$

$$M_{11}^{10} = \cos\eta_6 \quad ,$$

and

$$M_{11}^{11} = -\sin\eta_6 \quad .$$

The eigenvalues β_m are the solutions of the transcendental equation obtained by setting the determinant of the matrix in Equation 2-47 equal to zero. To obtain the remaining coefficients C_m of Equation 2-28, we exploit orthogonality and the initial condition. The eigenfunctions $X_{i,m}(x)$ satisfy the orthogonal relation [Özşik, 1993]

$$\sum_{i=1}^6 \frac{k_i}{\alpha_i} \int_{x_i}^{x_{i+1}} X_{i,m}(x) X_{i,n}(x) dx = \begin{cases} N_m, m = n \\ 0, m \neq n \end{cases} . \quad (2-48)$$

The normalization integral N_m and is given by

$$N_m = \sum_{j=1}^6 \frac{k_j}{\alpha_j} \int_{x_j}^{x_{j+1}} X_{j,m}^2(x) dx . \quad (2-49)$$

When $t = 0$

$$\theta_{t,i}(x,0) = \sum_{m=1}^{m=\infty} C_m X_{i,m}(x) = -\theta_{s,i}(x) . \quad (2-50)$$

Now multiplying both sides of Equation 2-50 by $\frac{k_i}{\alpha_i} X_{i,n}(x)$, integrating from x_i to x_{i+1} , and summing the result from $i = 1$ to 6 (the number of layers) yields

$$\left. \begin{aligned} - \sum_{i=1}^6 \frac{k_i}{\alpha_i} \int_{x_i}^{x_{i+1}} \theta_{s,i}(x) X_{i,n}(x) dx &= \sum_{i=1}^6 \frac{k_i}{\alpha_i} \int_{x_i}^{x_{i+1}} \sum_{m=1}^{m=\infty} C_m X_{i,m}(x) X_{i,n}(x) dx \\ &= \sum_{m=1}^{\infty} C_m \sum_{i=1}^6 \frac{k_i}{\alpha_i} \int_{x_i}^{x_{i+1}} X_{i,m}(x) X_{i,n}(x) dx \\ &= 0 + 0 + \dots + C_m N_m + 0 + 0 + \dots \end{aligned} \right\} . \quad (2-51)$$

Thus

$$C_m = -\frac{1}{N_m} \sum_{i=1}^6 \frac{k_i}{\alpha_i} \int_{x_i}^{x_{i+1}} \theta_{s,j}(x) X_{im}(x) dx \quad . \quad (2-52)$$

At this point all of the parameters needed to compute $\theta_{i,j}(x,t)$ from Equation 2-28 are known. The complete solution of the transient problem is given by Equation 2-21.

The C++ program *homog.cpp* listed in Appendix A is implemented using the preceding results to determine the temperature profile through the thermal radiation detector. A parametric study is performed to determine the optimum value of the thickness of the actual thermal impedance layer (Parylene). The influence of the contact conductance on the accuracy of the results obtained assuming perfect contact between layers is also considered.

2.3 Results

The actual values of the contact conductances are currently unknown for the fabrication technique (sputtering) anticipated for the notional detector. Further studies of the type being pursued by Sorensen will be necessary in order to determine these values. The models developed in the current chapter are anticipated to be an essential tool of Sorensen's research. The current objectives are to simulate the thermal behavior of the detector using different assumed values of the contact conductances to investigate the sensitivity of the overall behavior to this parameter. The bulk properties of the materials are used in this preliminary study. Assuming continuum mechanics, the thermal properties of thin-film layers are known to be a function of the layer thickness [Nath and Chopra, 1974; Kelemen, 1976; and Kumar et al, 1994]. However, thin-film properties for the materials in this investigation are currently unavailable. This is the topic of Chapter 3.

Figures 4 and 5 show, respectively, the transient temperature distribution of the detector with perfect contact and with imperfect contact conductance (in which case the contact conductance is arbitrarily set at 50,000 W/m² K for the six interfaces). This assumed value of contact conductance produces an increase of the temperature at all the locations

of the detector, as shown in Figure 5. The temperature is uniform across each junction and discontinuous at the interfaces for the non-perfect thermal contact between layers.

Figure 6 presents the steady-state response of the detector for different values of contact resistance as well as for perfect contact. As expected, the lower contact conductance results in a higher overall temperature rise at the active junction. It is apparent that the contact resistance effect, if present, cannot be neglected without underestimating the response of the detector. Also, the curious situation in Figures 5 and 6 in which the two components of the thermocouple junction are at different temperatures raises a question about how to interpret the temperatures in terms of the thermoelectric effect.

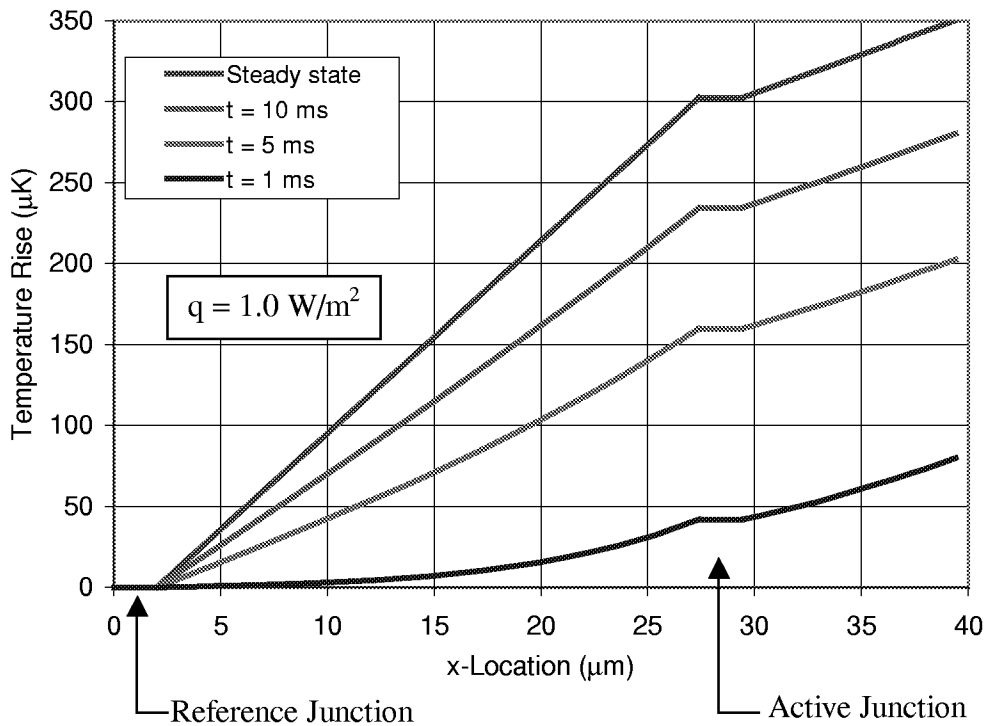


Figure 4: Temperature response of the notional detector of Figure 1 with perfect thermal contact between all layers.

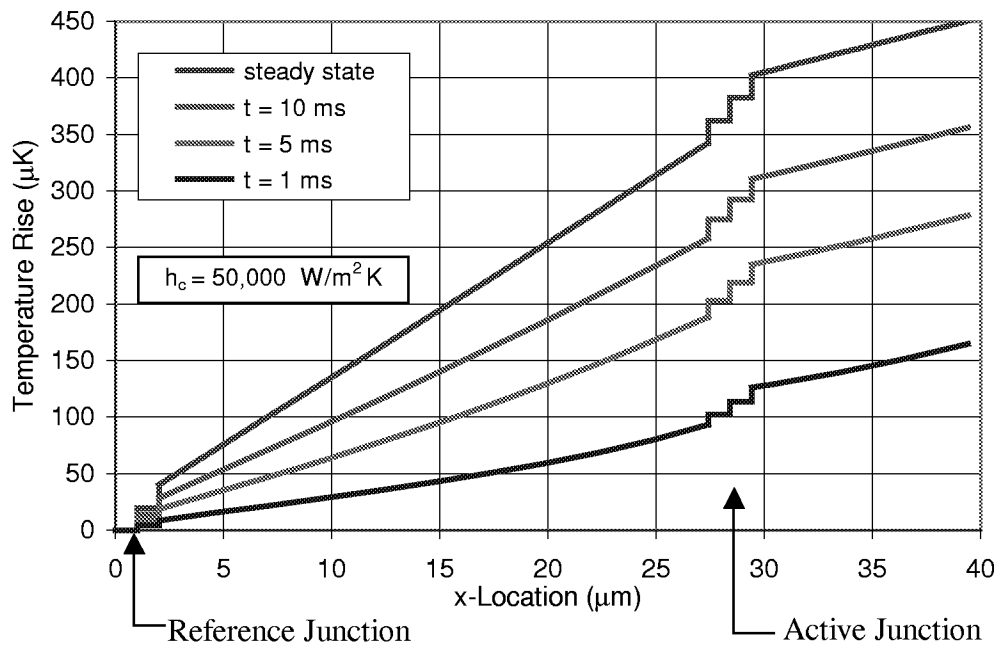


Figure 5: Temperature response of the notional detector of Figure 1 with a uniform thermal contact resistance between the layers.

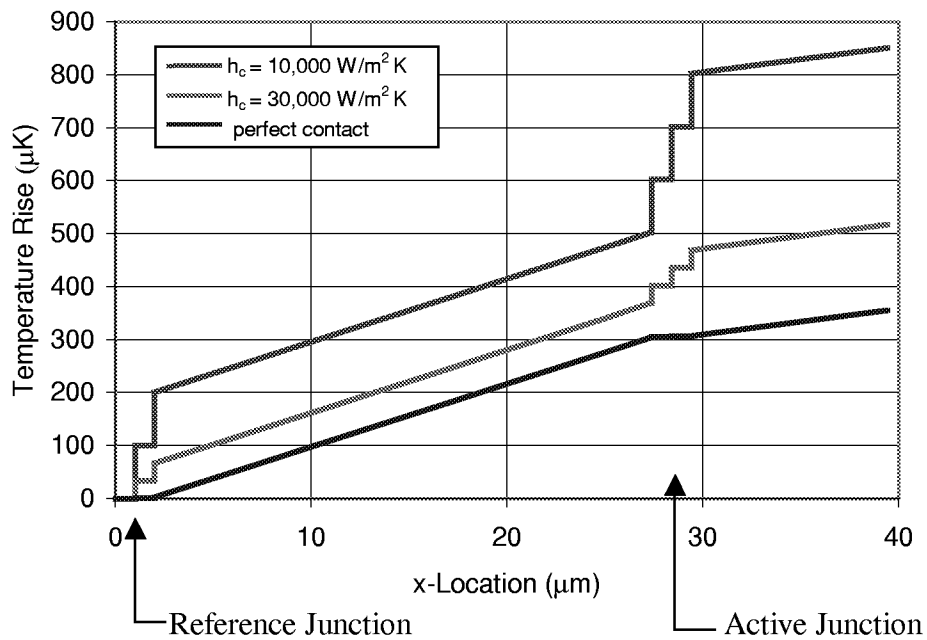


Figure 6: Steady-state temperature response of the notional detector of Figure 1 for different values of interlayer contact conductance.

The transient temperature response of the active junction, when the detector is subjected to a uniform heat flux of 1 W/m^2 on the upper surface of the absorber layer, is shown in Figure 7. The response is quasi-first order. The time constant is defined as the time for the temperature to undergo 63 percent of the temperature change from the initial to the steady-state value. The responsivity of the detector is the difference between the steady-state temperature of the active junction and that of the reference junction provoked by the heat flux. Figure 8 shows a linear increasing dependence of the responsivity on the thickness of the thermal isolation layer. However, the time constant also increases with thickness.

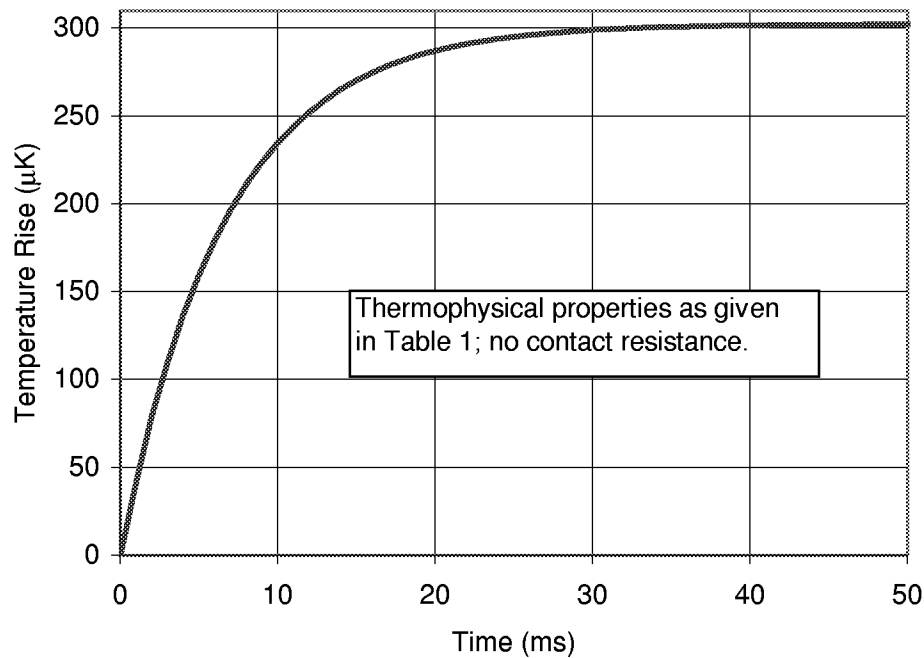


Figure 7: Transient temperature response of the active junction of the notional thermal radiation of Figure 1 detector with no contact resistance (thermophysical properties given in Table 1).

The use of less dense materials such as Larc-Si and aerogels, having superior thermal insulation properties, is anticipated to be the subject of future investigations. These

materials could possibly lead to a lower thermal capacitance for a layer of equal thickness, resulting in both a faster time response and a higher responsivity. One of the problems with these new materials is that their thin-film thermal properties are unknown.

The numerical model developed in the current chapter is modified in Chapter 4 in order to take into account a nonhomogeneous thermal impedance layer consisting of a mixture of aerogel and carbon, or a mixture of Larc-Si and carbon, or a mixture of Parylene and carbon.

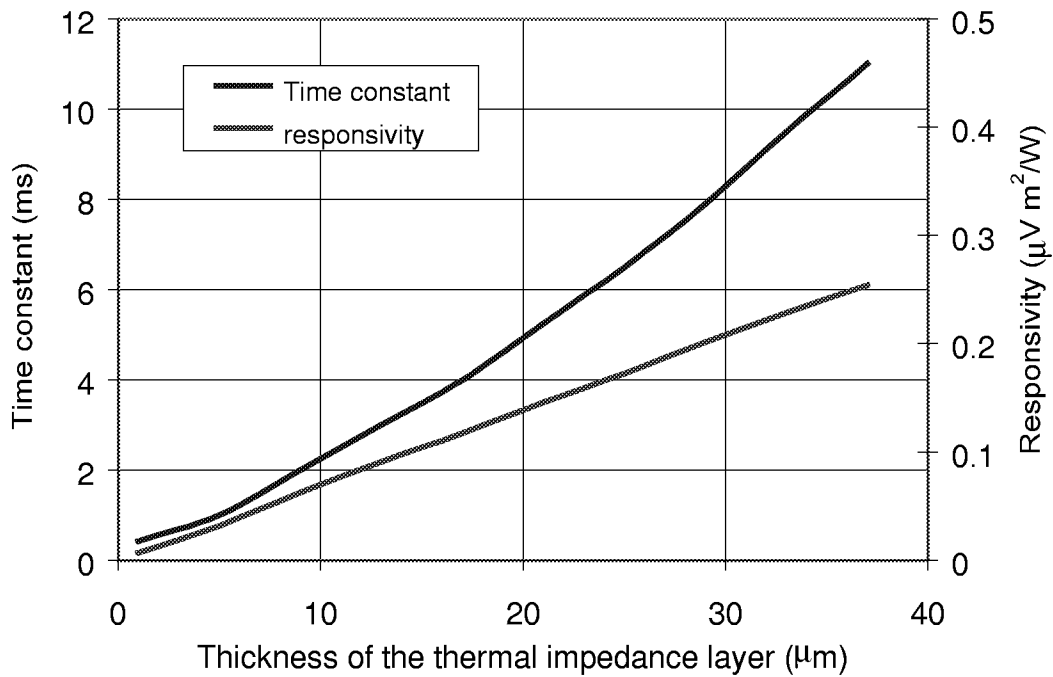


Figure 8: Time constant and responsivity of the notional detector of Figure 1 and Table 1 as a function of the thickness of the thermal impedance layer.

Chapter 3: The Thin-Film Effect

3.1 Review of thin-film heat transfer

In Chapter 2 the effect of contact resistance on detector performance was considered. In the current chapter we take up the question of the possible departure of thermophysical properties from their bulk values due to the so-called thin-film effect.

The heat conduction mechanism occurs in solids through collisions among phonons and electrons. In metals the main energy carriers are free electrons, while in insulators and semi-conductors, the energy is mainly carried by phonons. The macroscale heat transfer theories such as heat diffusion given by Fourier's law fail to describe the heat transfer process in microstructures if they are not used appropriately. The classical Fourier's law may be written

$$q = -k\nabla T \quad , \quad (3-1)$$

where q is the heat flux, k is the thermal conductivity and, ∇T is the local temperature gradient.

In situations where the characteristic length or/and characteristic time of a structure approaches, respectively, the mean free path or the mean free time of the main energy carrier, microscale heat transfer models are more appropriate. The classical macroscopic Fourier's law defined by Equation 3-1 breaks down because the definition of thermal conductivity depends on the existence of a gradient of temperature within the structure

[Majumdar, 1993]. The macroscopic models assume that the physical structure is so large and the time scale sufficiently long that sufficient collisions occur between the energy carriers as to assure that a local thermodynamic equilibrium is reached. In fact, the very concept of temperature at a given point is strictly defined only under the condition of local thermodynamic equilibrium. Therefore a meaningful temperature can be defined only at points separated by at least the mean free path of the energy carriers [Bejan, 1988]. We conclude that for heat conduction across a thin-film layer whose thickness approaches the order of magnitude of the mean free path, the thermal conductivity of the material cannot be defined as given by Equation 3-1. Because an insufficient number of heat carriers are present within the material, the temperature field becomes discontinuous through the layer and the temperature gradient concept loses its physical meaning within the layer. Microscale heat transfer can occur either in length scale or in time scale or in both scales. The two-step phonon-electron interaction model, the phonon-scattering model, the phonon radiative model, and the thermal wave model are some of the available microscale heat transfer models and are discussed by Tzou [1997].

An important issue of microscale heat transfer is the dependence of the thermophysical properties of thin-films on the microstructure of those films. In a 1984 effort, Decker et al. report that the measurements of the thermal conductivities of SiO_2 and Al_2O_3 thin films are apparently one or two orders of magnitude lower than those for the corresponding bulk materials. They also report that the thickness dependence is more pronounced for thermal conductivity than for the heat capacity and density in dielectric thin-films. Nath et al. [1974] report similar behavior by measuring the thermal conductivity of copper films ranging in thickness from 400 to 8000 Å in the temperature range 100-500 K. This decrease is attributed to a structural disorder inside the thin film layer, to a large interface thermal resistance, or to the limitation of the mean free path. Orain et al. [1998] also report a decrease of the thermal conductivity of ZrO_2 films with thickness ranging from 750 to 10,000 Å deposited on Al_2O_3 substrates.

Based on kinetic theory, the thermal conductivity of dielectrics and semiconductors is given by [Zima, 1960]

$$k = \frac{1}{3}Cvl \quad , \quad (3-2)$$

where C is the phonon specific heat, v is the speed of sound, and l is the phonon mean free path.

Equation 3-2 shows that the thermal conductivity is directly proportional to the mean free path of the main energy carrier. In thin films the mean free path is reduced from its bulk value because of the scattering on the boundaries, and thus so is the thermal conductivity. Also the mean free path being smaller in the transverse dimension of the film, the thermal conductivity in that direction is smaller than that in the longitudinal direction. For a film thickness much larger than the mean free path, the scattering being small, the decrease of the thermal conductivity by scattering can be neglected. From Equation 3-2, it is clear that the computation of an effective thermal conductivity of the thin film requires the knowledge of the mean free path of the main heat carrier. However the contradiction of using Equation 3-2 to explain departures from bulk thermal behavior in a mean free path regime where Fourier's law itself probably does not apply is obvious and must be recognized.

Kumar et al. [1994], using the Boltzmann transport theory, derived closed-form expressions that predict the reduction in the longitudinal thermal conductivity (in the direction parallel to the plane bounding the thin film) of thin metallic films due to boundary scattering. Flik and Tien [1990] argue that since the thermal conductivity is directly proportional to the mean free path, the reduction of the thermal conductivity should be equal to the reduction of the mean free path. They use geometric assumptions to evaluate the reduction in the component of the mean free path along the longitudinal direction of the film due to the termination of the path lines at the boundaries. They derive for the longitudinal conductivity of a thin metallic film, assuming that the path lines originate uniformly along the transverse direction (direction normal to the plane bounding the thin film) of the thin film,

$$\frac{k_{film}}{k_{bulk}} = 1 + \frac{2}{\pi} \delta \ln \frac{1 + \delta + s}{1 + \delta - s} - \frac{2}{\pi} \cos^{-1} \delta - \frac{2}{3\pi} \frac{1}{\delta} (1 - s^3), \quad \delta < 1, \quad (3-3)$$

and

$$\frac{k_{film}}{k_{bulk}} = 1 - \frac{2}{3\pi} \frac{1}{\delta} \quad , \quad \delta > 1, \quad (3-4)$$

where δ is the ratio of the film thickness to the mean free path, and $s = (1 - \delta^{-2})^{1/2}$ in Equation 3-3.

Figure 9 shows the ratio of the “thin-film” longitudinal conductivity to the bulk conductivity for a range of thicknesses determined using Equations 3-3 and 3-4. The figure clearly shows the dependence of the thin-film thermal conductivity on the ratio of the thin-film thickness to the mean free path length.

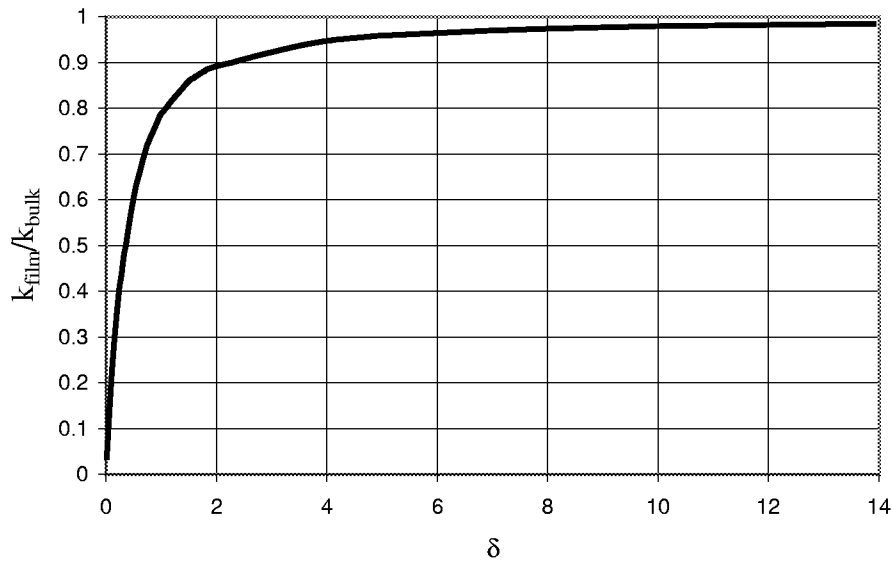


Figure 9: The ratio of the longitudinal thin-film to the bulk conductivities as defined by Equations 3-3 and 3-4.

3.2 The thin-film thermal conductivity anomaly as a roughness effect

The thermal conductivity is a parameter that has a direct influence on the accuracy of models of heat conduction processes. The experimental studies reported in the open literature that attempt to recover the effective thermal conductivity of a thin film fail to

take into account the roughness of the thin film. They seem to assume that the thin-film is completely smooth or that its roughness is negligible. Closed-form equations of the thermal conductivity of thin films, such as Equations 3-3 and 3-4, require the knowledge of the mean free path of the energy carrier, a property that is not available in the literature for the materials of the notional thermal radiation detector. When the film layer is very thin (on the order of microns), its relative roughness can no longer be neglected. It may be hypothesized that roughness plays an important role in the apparent deviation of the properties of individual layers from their bulk values. In other words, reported deviations of thermal properties from the bulk values may be an artifact of experimental techniques that ignore the possibility of roughness effects.

The objective here is to determine whether or not unsampled surface roughness could possibly explain the observed decrease of thermal conductivity. In fact, no effective conductivity data are available in the open literature for the special materials, such as Larc-Si and Zinc-antimonide, that are being considered for use in the notional detector. One can then imagine performing an experiment to define the statistical description of surface roughness for a given sample and then using this information and the bulk thermal conductivity with an appropriate model to predict the effective thermal conductivity.

A statistical technique is required for solving the heat transfer equations describing the roughness effect for very complicated surface topographies.

3.2.1 The random walk approach

The Monte-Carlo method, also called the method of statistical trials, is a system of techniques that enables complex physical models of problems to be solved in relatively simple manners. The computer is instructed to do most of the work. This approach is limited only by the availability of adequate computer resources (mainly speed). In Monte-Carlo methods, instead of directly solving an analytical problem, one “plays a game” following rules similar to those governing the actual physical process. The game has the same outcome as the actual physical process but is in some sense easier to play.

The random walk is a Monte-Carlo method used to solve boundary-value and initial condition problems. The random walk method enables problems with irregular geometries and multiple dimensions to be solved using algorithms that are quite simple compared to other methods such as the finite difference or finite element methods.

3.2.1.1 Presentation of the technique

In the current study, a two-dimensional steady-state heat conduction problem with no internal heat generation is considered.

The mathematical formulation of the problem is

$$\frac{\partial^2 T(x, y)}{\partial x^2} + \frac{\partial^2 T(x, y)}{\partial y^2} = 0 \quad , \quad (3-5)$$

with either

$$T = f(x, y) \quad (3-6)$$

or

$$q(x, y) = 0 \quad (3-7)$$

specified on the boundary Γ . That is, the kind of boundary condition considered is either specified boundary temperature or an insulated boundary.

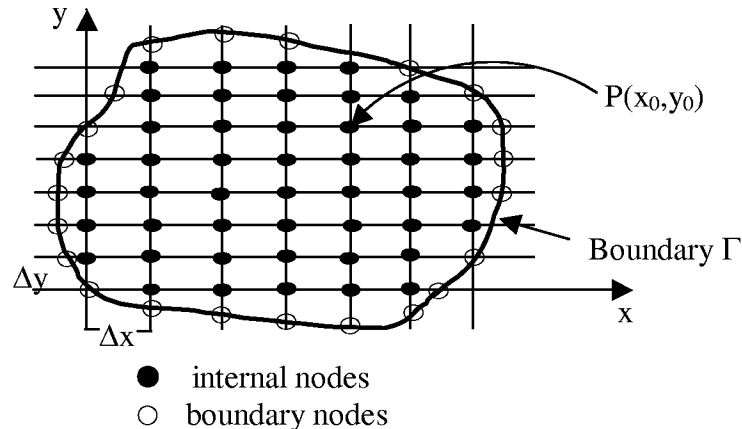


Figure 10: Network of nodes for an arbitrary irregular geometry.

One would like to compute the temperature at a given point $P(x_0, y_0)$ in the two-dimensional domain limited by the boundary Γ , as illustrated in Figure 10. The random walk technique works as follow.

Starting at $P(x_0, y_0)$ a random number uniformly distributed between zero and unity is drawn to determine in which direction to “step”. In a two-dimensional net, one can step with equal probability either to the north, the south, the east or the west with a step size Δx in the x direction and Δy in the y direction. Having arrived at the appropriate neighboring node, the same process is repeated to determine the direction of the next step. This process is repeated until a boundary node is reached. Having arrived at a node whose location is approximately on the boundary, the next step depends on the type of boundary condition: either a specified temperature or an insulated boundary is considered. When an insulated boundary node is reached, the next node in the random walk is identical to the previous node, as in specular reflection. When a boundary node with a specified temperature is reached, a counter ζ_0 is incremented by the value of the temperature specified at that node. Then the whole process recommences at point $P(x_0, y_0)$ and is repeated until a large number N of random walks has been completed. Finally, after a sufficiently large number of random walks initiated a point $P(x_0, y_0)$, the temperature at point $P(x_0, y_0)$ is estimated as ζ_0/N .

The precision of the temperature computed this way depends on the value of the number of random walks N and the fineness of the grid. The larger N , the more accurate the result for a sufficiently fine grid. On the other hand increasing either N or the fineness of the grid increases the computational time. A trade-off clearly exists between the precision sought and the computer time needed to get that precision, assuming the grid is sufficiently fine to provide the desired precision.

Another problem of using random walk methods is the lack of reproducibility of the results if N is not sufficiently high. When running the same problem several times, one never gets exactly the same results. This is due to the difference in the sequences of random numbers generated for each experiment.

The interested reader is referred to the book by Shreider [1966] for additional information on this technique.

The flowchart given in Figure 11 illustrates the random walk technique in a two-dimensional heat condition problem without internal heat generation.

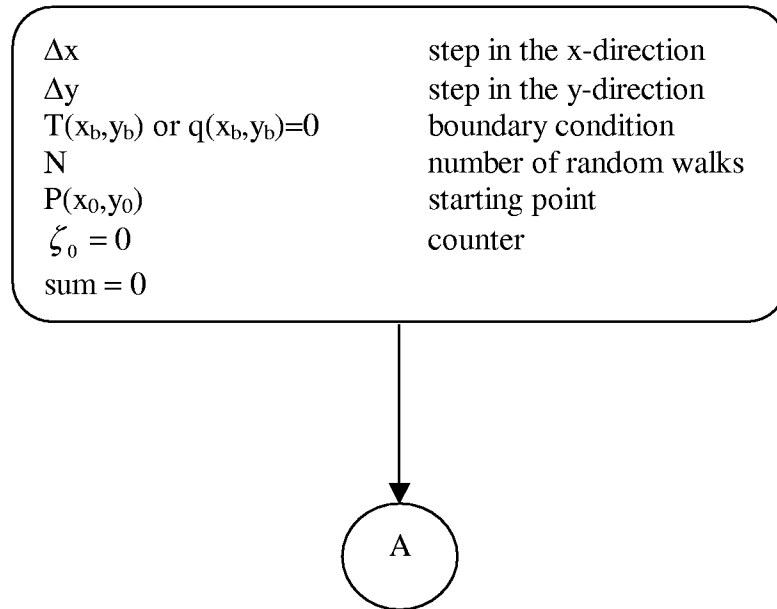


Figure 11: Flowchart of a two-dimensional random walk (continued on next page).

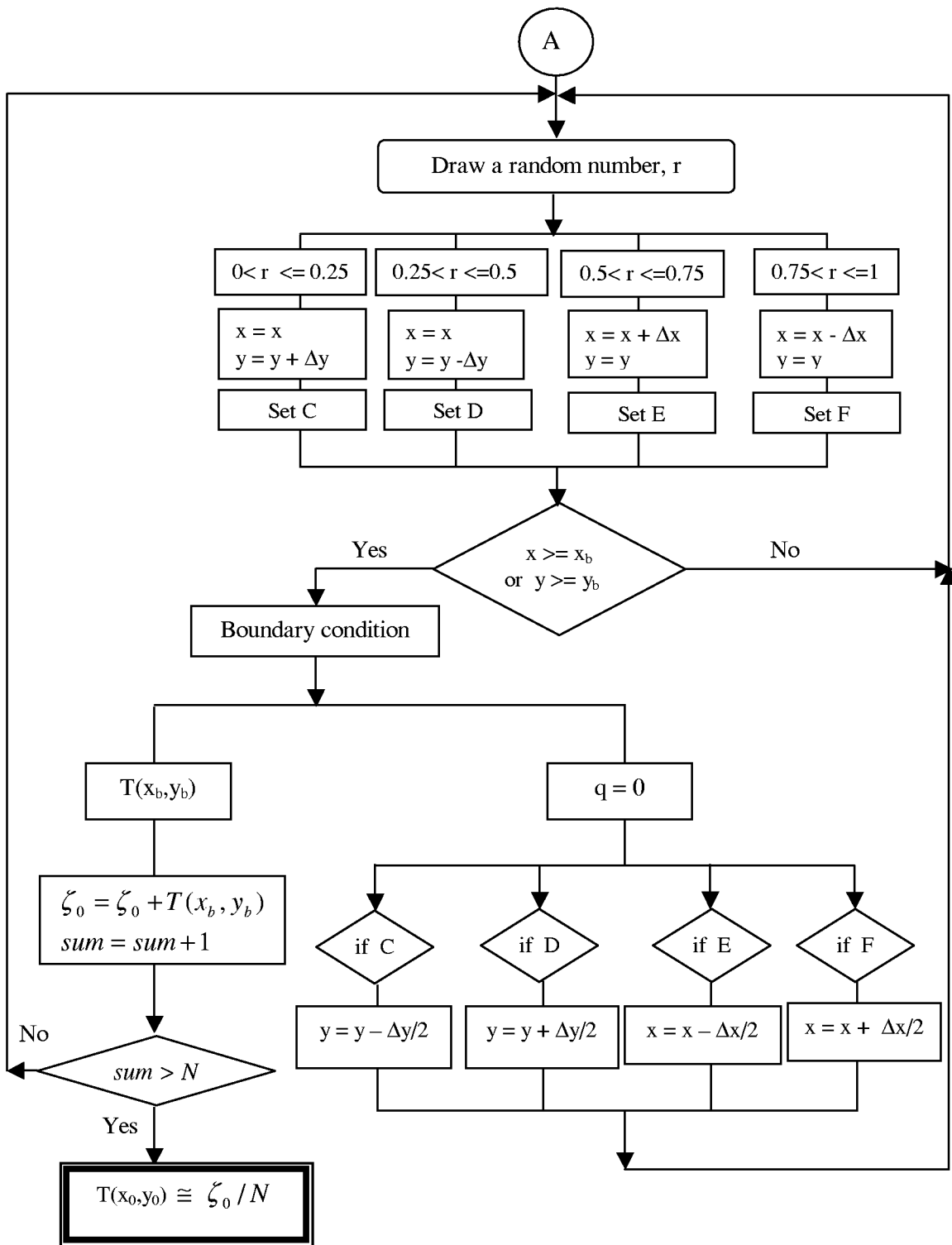


Figure 11 (continued): Flowchart of a two-dimensional random walk.

3.2.1.2 Results

The program *randwalk2d.cpp* listed in the Appendix B can be used to determine the temperature profile for different geometries. The random walk method developed is benchmarked using a problem for which exact closed-form solutions are available.

The benchmark problem considered using this technique is one-dimensional steady-state heat conduction in a flat plate, as illustrated in Figure 12.

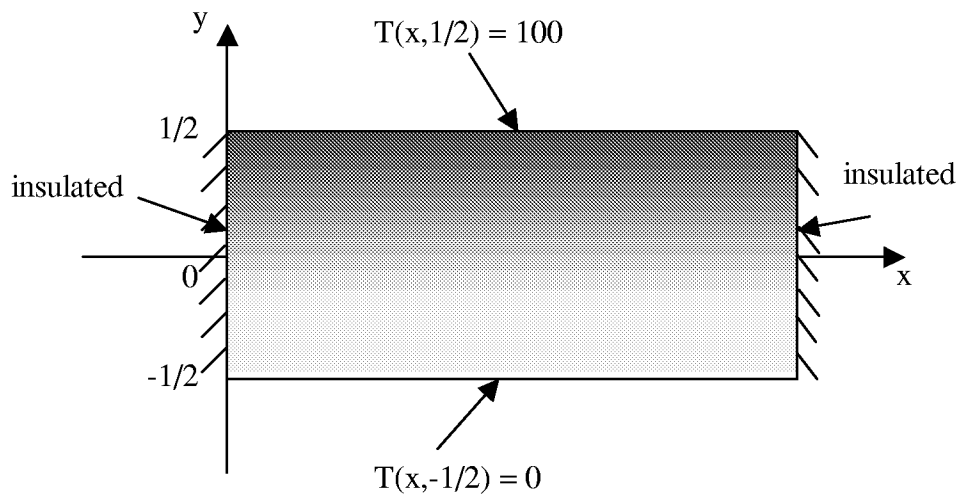


Figure 12: One-dimensional, steady-state heat transfer in a flat plate.

The analytical temperature distribution is

$$T_{exact}(y) = 100y + 50 \quad . \quad (3-8)$$

It is convenient to define an error ε

$$\varepsilon = \frac{1}{n_y} \sum_{i=1}^{n_y} \frac{|T_{rw}(y_i) - T_{exact}(y_i)|}{T_{exact}(y_i)} \times 100\% \quad . \quad (3-9)$$

In Equation 3-9, $T_{rw}(y)$ is the value of the temperature obtained using the random walk method and n_y is the number of discrete divisions in the y direction.

The random walk code is executed for different values of the number of random walks, N . The reproducibility at a given N is studied by running the code several times with different starting seeds in the pseudorandom number generator used to draw the required random number. The error ε is computed for each run.

Table 2 displays the results obtained for five runs at a given value of N and shows that the error is different from one run to the next. The lack of reproducibility from one run to the next is illustrated in Figure 13.

Table 2: Error values for different runs of the random walk solution to the problem defined by Figure 11 with $n_y = 50$.

Number of random walks, N	error, ε (% , Equation 3-9), $n_y = 50$				
	first run	second run	third run	fourth run	fifth run
50	19.26	17.91	16.91	16.16	10.57
100	12.48	7.07	10.22	11.61	10.53
250	8.72	5.71	8.67	6.34	7.03
500	5.81	4.19	3.33	4.29	5.20
1000	4.20	3.78	2.90	3.27	2.76

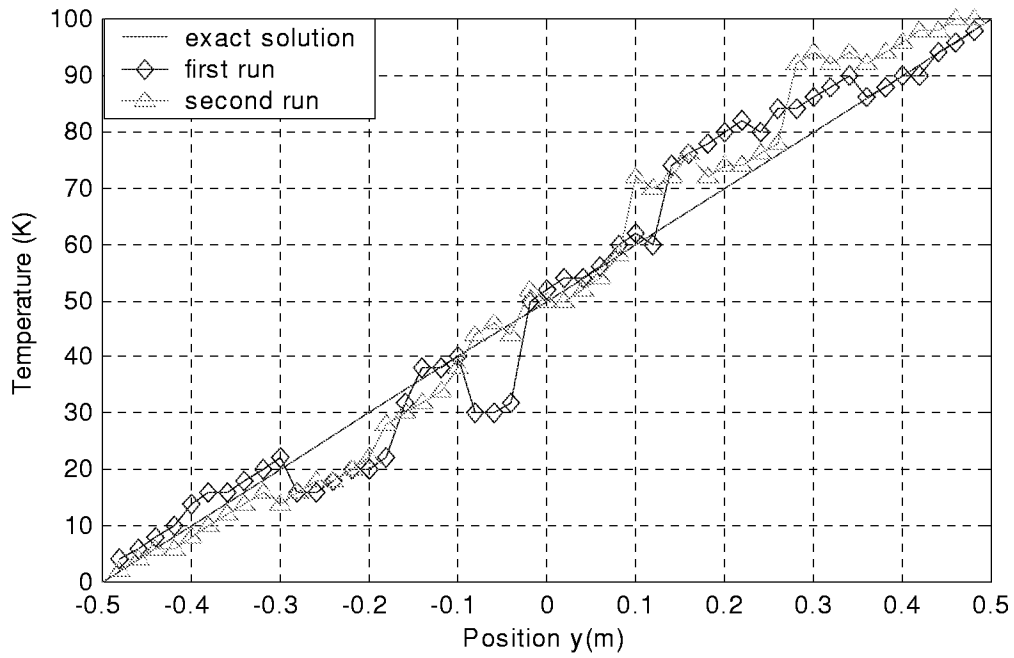


Figure 13: First two runs for $N = 50$ compared with exact temperature distribution for the problem defined by Figure 12.

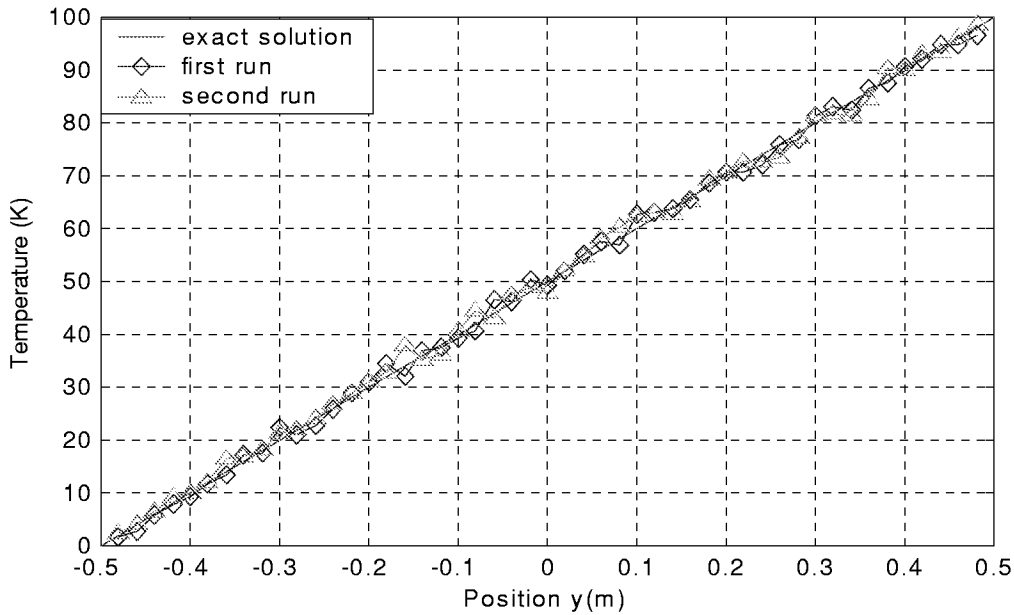


Figure 14: First two runs for $N = 1000$ compared with the exact solution for the problem defined by Figure 12.

Table 2 and Figure 14 show that the lack of reproducibility decreases significantly when the number of random walks increases. The value of n_y is fifty for each of these experiments.

Table 3 presents the influence of the number of random walks on the machine time (SGI; Model: Indigo2 XZ, Extreme; Operating System: IRIX Release 6.5) and on the mean error. The machine time is the time it takes to complete the computation, and the mean error $\langle \varepsilon \rangle$ is obtained by setting T_{rw} in Equation 3-9 equal to the arithmetic mean value of T_{rw} , $\langle T_{rw} \rangle$, for all the runs; that is,

$$\langle \varepsilon \rangle = \frac{1}{n_y} \sum_{i=1}^{n_y} \frac{|\langle T_{rw}(y_i) \rangle - T_{exact}(y_i)|}{T_{exact}(y_i)} \times 100\% \quad (3-10)$$

and

$$\langle T_{rw}(y_i) \rangle = \frac{1}{n_r} \sum_{i=1}^{n_r} T_{rw}(y_i) \quad , \quad (3-11)$$

where n_r is the number of runs for a given number of random walks, N .

As one would anticipate, by increasing the number of random walks, the machine time increases and the result becomes more accurate. Once again the number of y divisions, n_y , is fifty for each of these numerical experiments.

Table 3: Influence of the number of random walks on the machine time and the mean error for the problem defined by Figure 12 with $n_y = 50$.

Number of random walks, N	Machine time (s)	Number of runs, n_r	Mean error (%)
50	8	5	7.88
100	17	5	3.61
250	44	5	2.90
500	88	5	2.52
1000	176	5	1.73
5000	885	1	1.54

Figure 15 shows a comparison between the result obtained for just one run with 5000 random walks and the exact solution. The error being only about 1.5 percent, the temperature obtained by the random walk technique can be acceptably accurate.

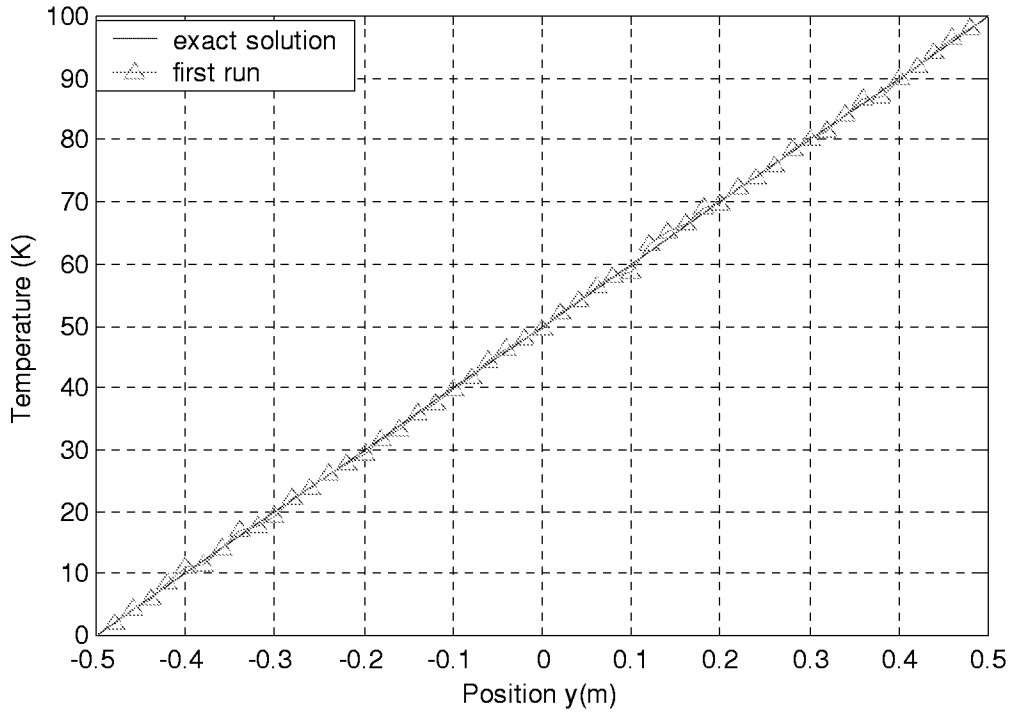


Figure 15: Comparison of the temperature distribution computed using the random walk method with $N = 5000$ and $n_y = 50$ with the exact solution for the problem defined by Figure 11 with.

The two-dimensional random walk technique has also been used to compute the temperature distribution when surfaces are modeled as trigonometric functions, as illustrated in Figure 16.

Figure 17 represents the temperature profile at $x = 5 \mu\text{m}$ in Figure 16 computed using the random walk method for different values of the number of walks N .

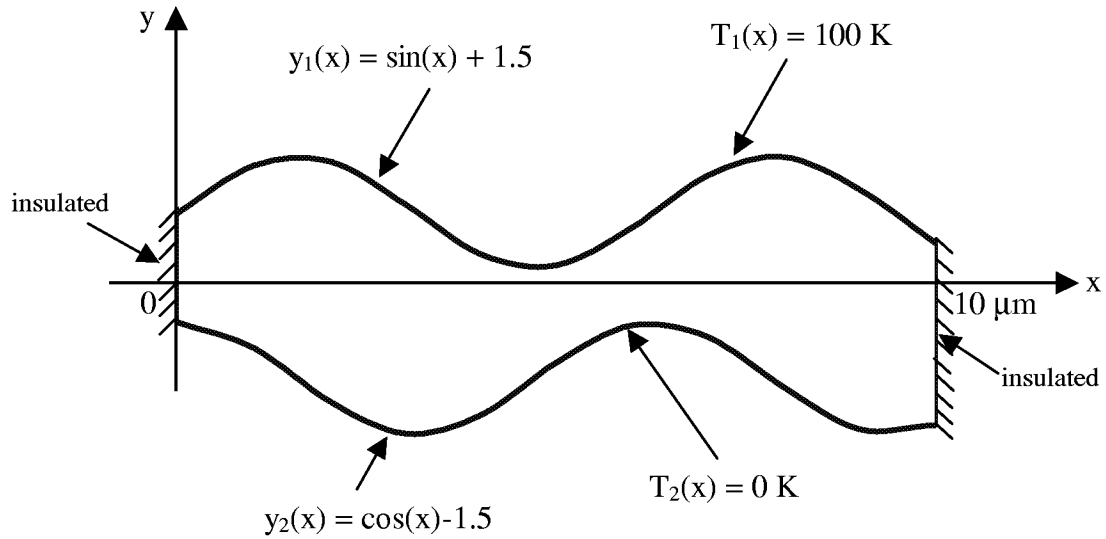


Figure 16: Irregular geometry representing a layer of variable thickness.

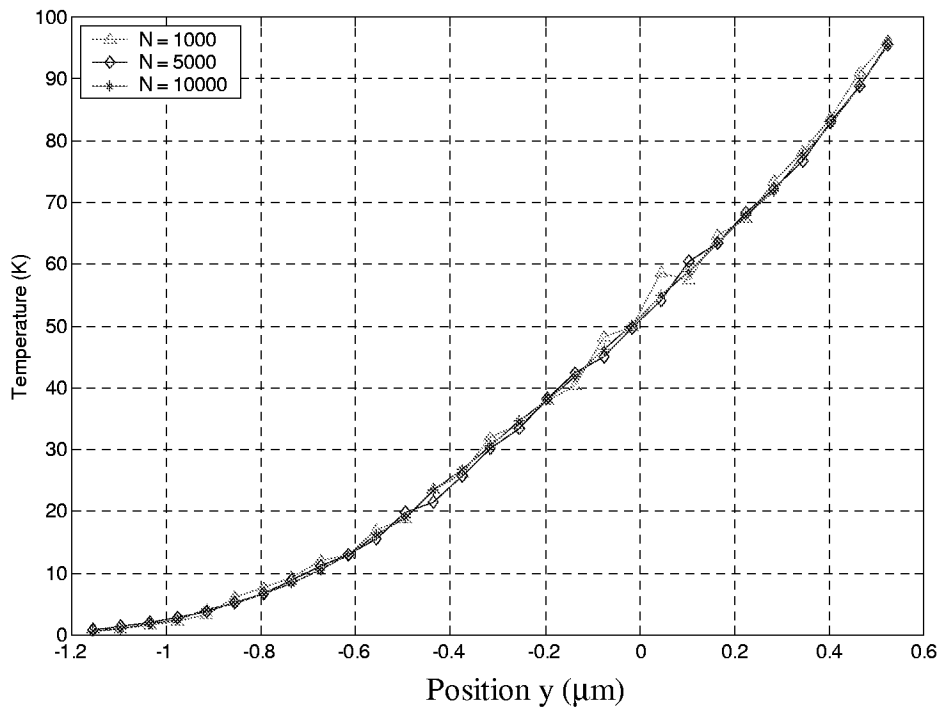


Figure 17: Comparison of the temperature distribution computed using the random walk method at $x = 5 \mu\text{m}$ in Figure 16 with $n_y=50$, $N = 1000, 5000$, and 10000 .

3.2.2 Effective thermal conductivity of a thin-film layer of irregular thickness.

The investigation of the effective thermal conductivity of a thin-film layer based on a roughness effect begins with the simple two-dimensional model illustrated in Figure 18. The idea is that if the results obtained using this model are consistent with the expected trend, that is a decrease of the thermal conductivity of the thin-film as the roughness increases, then more realistic surfaces would be considered. It is convenient to use a finite difference model in order to determine the temperature distribution for the geometry in Figure 18. The finite difference method is conceptually simple for problems having regular rectangular boundaries. It involves the use of nodal networks, finite difference approximations for derivatives in space and time, standard energy conservation formulation concepts, and computer solution of systems of algebraic nodal equations. The control volume approach is used for the discretization of the governing equations. The C++ code *eff_cond.cpp* listed in Appendix C and developed for computing the temperature profile using the finite difference method in a two-dimensional regime without internal heat generation is adapted from Vick [1998]. If this study indicates that an unsampled roughness effect can explain the observed thin-film effect, then the random walk method will be used to study more realistic geometries.

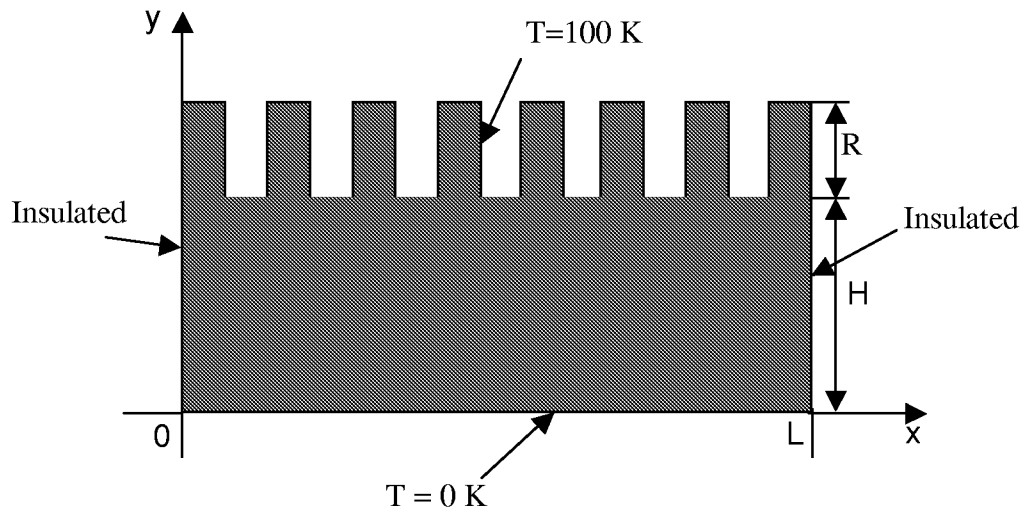


Figure 18: Model of a hypothetical two-dimensional rough surface.

Here, the effective conductivity k_{eff} of a real surface is defined as the conductivity of a hypothetical plane surface having the following three properties:

- the same length L as the surface in Figure 18,
- the same total heat flux as the problem defined by Figure 18,
- a uniform thickness of $H + R/2$, where H and R are defined in Figure 18.

A discretized version of Figure 18 is shown in Figure 19. Because the problem is two-dimensional, the total heat flux in the y direction is approximated using the bottom row of control volumes in the Figure 19. Then for a given control volume at the bottom of Figure 19, the heat flux through the i th heat flow channel is approximated by

$$Q_i \cong -k_{bulk} \frac{T(x_i, \Delta y/2) - T_1}{\Delta y/2} \Delta x_i \quad (\text{W/m}). \quad (3-12)$$

The total heat flux is then approximated by

$$Q_T = \sum_1^{ii} Q_i = 2 \frac{k_{bulk}}{\Delta y} \sum_1^{ii} [(T(x_i, \Delta y/2) - T_1) \Delta x_i] \quad (\text{W/m}), \quad (3-13)$$

where ii , is the number of control volumes in the x direction, and k_{bulk} is the bulk conductivity of the material.

The total heat flux of the hypothetical flat surface is given by

$$Q = -k_{eff} L \frac{T_2 - T_1}{(H + R/2)} \quad (\text{W/m}). \quad (3-14)$$

Equating Equations 3-13 and 3-14 yields

$$\frac{k_{eff}}{k_{bulk}} = \frac{(H + R/2)}{L} \frac{2}{T_2 - T_1} \sum_1^{ii} [(T(x_i, \Delta y/2) - T_1) \Delta x_i] \quad . \quad (3-15)$$

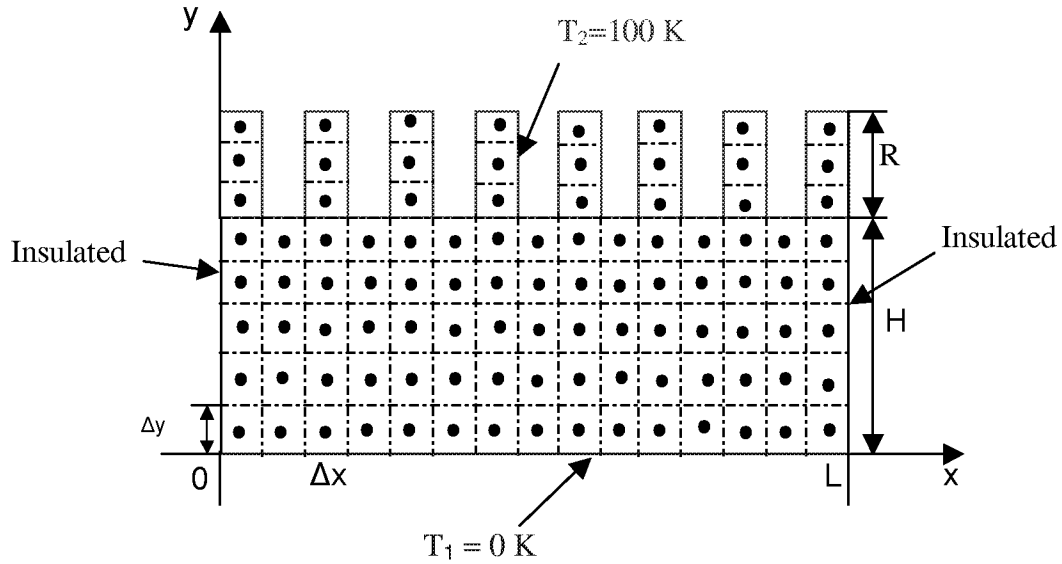


Figure 19: Control volume discretization of the hypothetical two-dimensional rough surface of Figure 18.

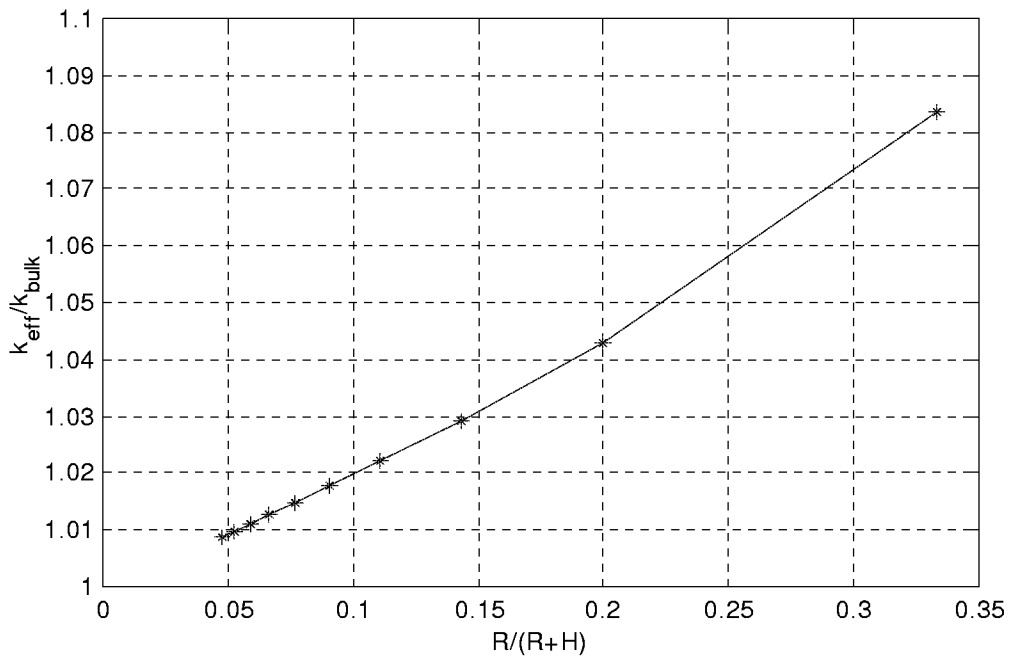


Figure 20: ratio of the effective thermal conductivity to the bulk thermal conductivity for the problem defined by Figures 18 and 19 with forty control volumes in the x direction and $L/H = 5$.

In order to study how the roughness, represented by the nondimensional quantity $R/(R+H)$ influences the ratio k_{eff}/k_{bulk} , the value of R is set constant in the finite difference procedure and the ratio is computed for different values of H . Figure 20 illustrates the result obtained.

The trend of Figure 20 is completely the opposite of what is expected. That is if unsampled roughness is to account for the observed [Nath and Chopra, 1974; and Orain et al., 1998] behavior of effective thermal conductivity in thin-film layers, a decrease of the effective thermal conductivity is expected as the roughness increases. The effective conductivity for the model of Figure 19 exceeds the bulk value when the roughness increases, and approaches the bulk value as the surface becomes smoother. Looking more closely at the geometry Figure 18, one can see that when H becomes smaller compared to R , the surface at higher temperature T_1 is closer to the plane at temperature T_2 so that the local gradient of temperature is larger. The larger temperature gradient yields a higher total heat flux and therefore a higher effective conductivity.

We conclude that the approach used is unable to reproduce the trends reported in the literature. In other words, unsampled surface roughness cannot explain experimental results. Therefore, the random walk technique is not considered further for studies with more realistic surface models.

Evidently other approaches such as experimental measurements or parameter estimation techniques will have to be used to determine how the thermal conductivities for the materials of current interest are affected by the thin-film effect.

In Chapter 4 we investigate the effect on effective thermal and electrical conductivity of doping the thermal impedance layer with conducting material such as finely divided graphite.

Chapter 4: Effect of Doping the Thermal Impedance Layer with Conducting Particles

In the previous Chapter we investigated and rejected surface roughness as a possible explanation for the so-called “thin-film” effect. In this Chapter we consider the effect on thermal and electrical conductivity of doping the thermal impedance layer with finely divided carbon.

The NASA team led by Mr. Edward H. Kist, Jr., has proposed that the thermal impedance layer of the thermal radiation detector be doped with up to fifty percent by volume of finely divided graphite. The reason for this is to decrease the internal electrical resistance of the thermal impedance layer, thereby assuring the electrical connection between the two junctions of the thermal radiation detector. As stated before, the geometry and size of the detector preclude linking the two junctions by a more traditional conductor. Experiments carried out by Sorensen [1998] showed a decrease of the electrical resistance of thin layers of Larc-Si doped with powdered graphite. Minimization of the electrical resistance of this layer is a key factor for reducing an important noise source in radiation detectors. Johnson noise in an electric circuit is known to be directly proportional to the square root of its electrical resistance [Lenoble, 1993]. The noise sources in thermal radiation detectors are discussed by Lenoble [1993] and Haeffelin [1997].

An obvious concern is that reduction of the electrical resistance would also lead to reduction of the thermal resistance and concomitant reduction of the detector's

responsivity. The objective here then is to develop an analytical model that predicts the performance of the detector whose thermal impedance layer is doped with conductive particles. This situation is shown in Figure 21. The model is applied to the specific case of a Parylene impedance layer doped with carbon particles.

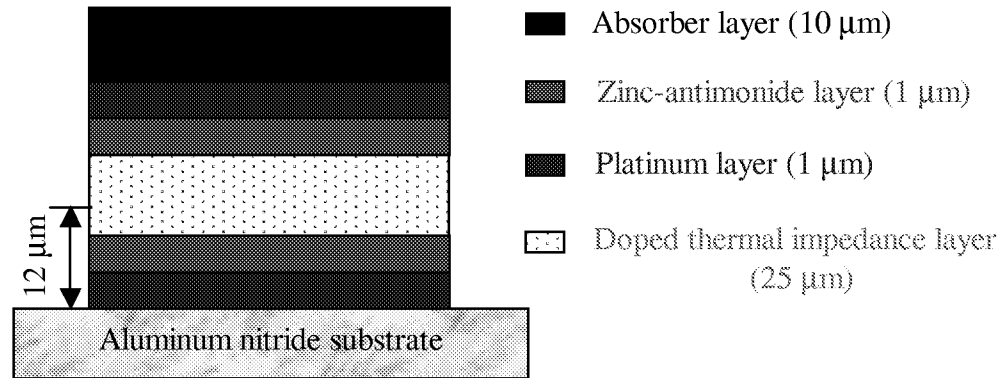


Figure 21: Detector geometry with graphite doped thermal impedance layer.

The behavior of the thermal radiation detector is studied first using a model of the detector derived from a model by Vick and Scott [1998] and then using micromechanical models.

4.1 Heat transfer in a heterogeneous material modeled as a coupled, two-step process.

4.1.1 Formulation

The transient thermal response of a heterogeneous material depends on the microstructure of the material. The one-dimensional heat transfer model developed by Vick and Scott considers relatively small spherical particles (the Biot number of less than 0.1) embedded in a matrix. In this model heat is first conducted to the matrix material from the boundaries and then transferred from the matrix to the particles through a contact

conductance. The particles are not in perfect thermal contact with the matrix material and they can receive heat only from the matrix. The boundaries of the thermal impedance layer in the current version of the model are the two zinc-antimonide layers of the active and reference junctions shown in Figure 21.

On the basis of an energy balance Vick and Scott have proposed that

$$C_m \frac{\partial T_m}{\partial t} = K \frac{\partial^2 T_m}{\partial x^2} - H(T_m - T_p) \quad (4-1)$$

and

$$C_p \frac{\partial T_p}{\partial t} = H(T_m - T_p) \quad (4-2)$$

for the doped matrix for one-dimensional transient heat flow.

In Equations 4-1 and 4-2 $C_m = (1-f)(\rho c)_m$ is the heat capacity of the matrix per total volume and $K = (1-f)k_m$ is the thermal conductivity of the matrix-particle system. $C_p = f(\rho c)_p$ is the heat capacity of the embedded particles per total volume, and f is the volume fraction of the embedded particles. The coupling coefficient between the matrix and the particles is $H = h(NA_p)$, where $A_p = \pi a^2$ is the surface area of a particle, h is the contact conductance, and N is the number of particles per volume.

This model is analogous to the two-step model developed by Tzou [1997] in order to describe the microscale heat transfer process for metals in which the electron gas is heated first and then the heat is transferred to the metal lattice. It holds for each of the six layers of the thermal radiation detector, but the number of particles is set equal to zero for layers with no carbon particles. The boundary conditions are a specified temperature at the base of the detector and a constant and uniform heat flux applied at the upper surface.

The coupled equations, Equations 4-1 and 4-2 are not solvable analytically. Vick and Scott used a fully implicit finite difference numerical approach to discretize those

equations. The fully implicit discretization makes the results unconditionally stable. The results of the discretization are

$$C_m \Delta x \frac{(T_{m,j}^i - T_{m,j}^{i-1})}{\Delta t} = K \frac{T_{m,j+1}^i - T_{m,j}^i}{\Delta x} - K \frac{T_{m,j}^i - T_{m,j-1}^i}{\Delta x} - H \Delta x (T_{m,j}^i - T_{p,j}^i) \quad (4-3)$$

and

$$C_p \Delta x \frac{T_{p,j}^i - T_{p,j}^{i-1}}{\Delta t} = H \Delta x (T_{m,j}^i - T_{p,j}^i) \quad (4-4)$$

where j and i are the indices of the nodes and time steps, respectively.

To solve these coupled equations, $T_{p,j}^i$ from Equation 4-4 is first substituted into Equation 4-3 and the resulting tridiagonal matrix is solved for the temperatures $T_{m,j}^i$ at each time step. The values of $T_{m,j}^i$ are then substituted into Equation 4-4 to compute the particle temperature $T_{p,j}^i$ within the thermal impedance layer.

The program *heterog.cpp* listed in Appendix D determines the temperature response of the detector for different values of the contact conductance between the carbon particles and the matrix material. The values of the contact conductance and the particle diameters are chosen so that the Biot number always remains small (less than 0.1). In this case the lumped capacity approximation is valid within each particle; that is, temperature gradients are negligible within a given particle.

4.1.2 Results

In all the cases considered in this chapter, the contact resistances between the different layers of the thermal radiation detector are assumed negligible, and the carbon particles are assumed to be uniform in size. It is recognized that this latter assumption would be difficult to realize in practice. However, the assumption approximates the situation in which a mean particle size is used to represent some size distribution. The contact

resistances between the layers forming the detector are neglected in order to focus on only one phenomenon at a time.

Studies of the effect of three parameters on detector response were carried out using the two-step model process. The three parameters are:

- the volume fraction, f , of the particles,
- the contact conductance between the particles and the matrix and
- the particle size.

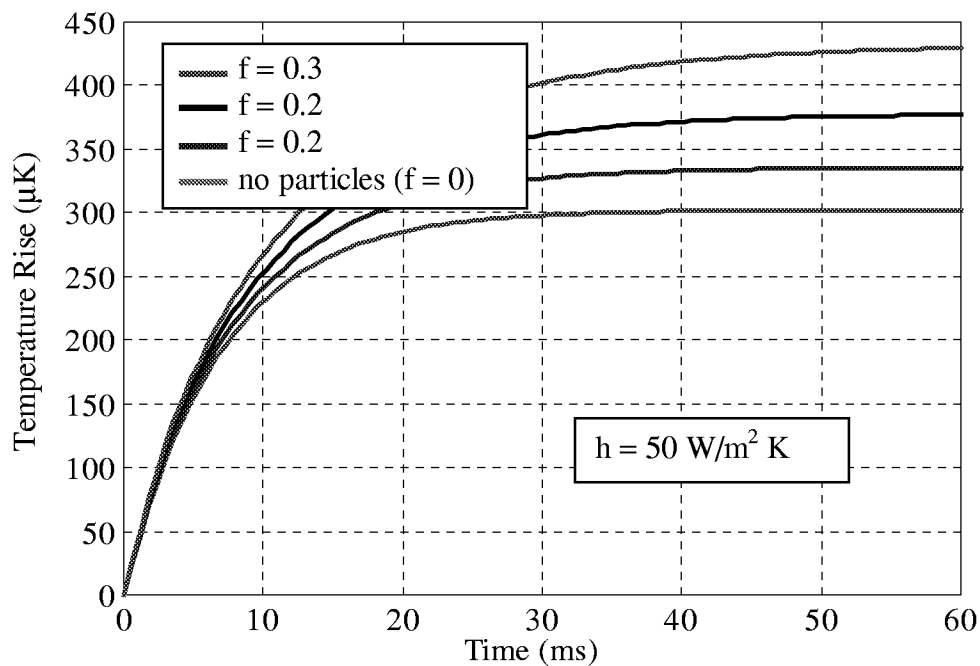


Figure 22: Temperature response of the active junction with $h = 50 \text{ W/m}^2 \text{ K}$.

The model developed here holds only for a matrix with dimensions much greater than a particle diameter and with a small volume fraction of particles within the matrix. Vick and Scott do not specify the volume fraction limit at which the model breaks down. Therefore the model is used here only for volume fractions of particles ranging between zero and thirty percent.

Figure 22 shows the transient temperature response of the active junction for four cases of particle volume fraction, f . The contact conductance between the particles and the matrix is $50 \text{ W/m}^2 \text{ K}$ in all four cases. The figure reveals an increase of the steady-state temperature of the active junction of the detector as the particle volume fraction increases. This result seems to be counterintuitive; that is, it is expected that the thermal impedance would decrease as the volume fraction of conductive particles increased.

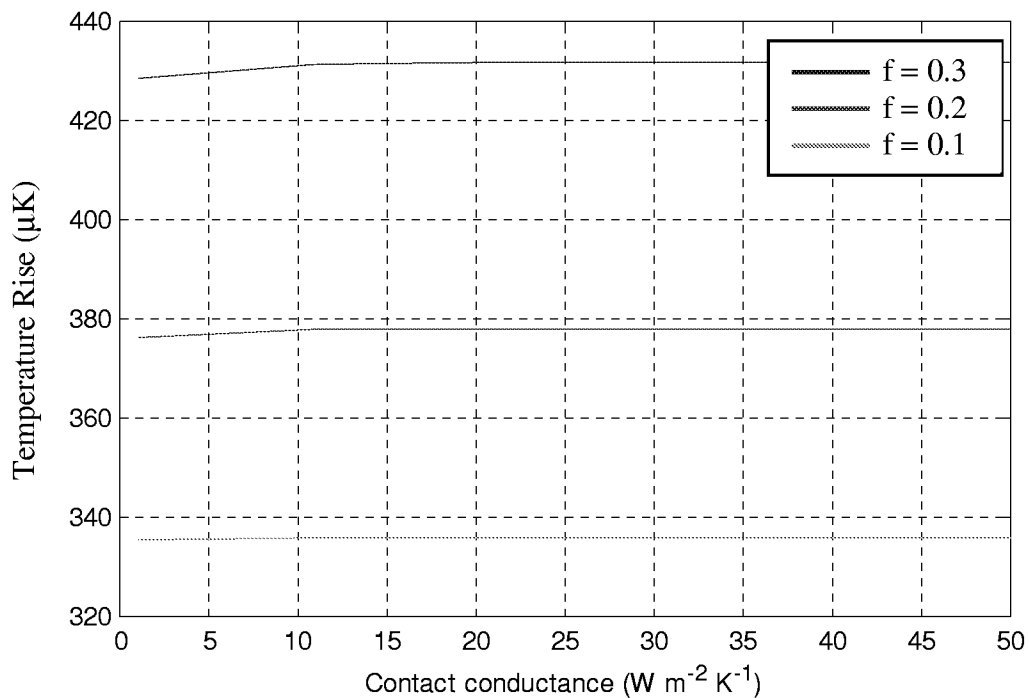


Figure 23: Effect of contact conductance between the particles and the matrix on the steady-state temperature rise of the active junction.

Figure 23 shows that the contact conductance between the matrix and the particles has negligible effect on the response of the thermal radiation detector. The greatest change of the response of the detector with respect to the contact conductance is less than one percent for the range of particle volume fractions considered in this study.

For the geometry and range of parameters investigated, the contact conductance has more effect on the temperature of the particles than on the temperature of the active junction of the detector, as shown in Figure 24. The heat is transferred from the matrix to the particles; therefore when the contact conductance increases, the time lag of the particles decreases. Note that the curve labeled “matrix” in Figure 24 actually consists of three superposed curves corresponding to the three values of h . Therefore it is clear that the contact conductance has little effect on the matrix temperature. The time lag of the particles decreases rapidly as the contact conductance increases. When h is about $10 \text{ W/m}^2 \text{ K}$ the time lag between the matrix and particle temperatures is effectively zero.

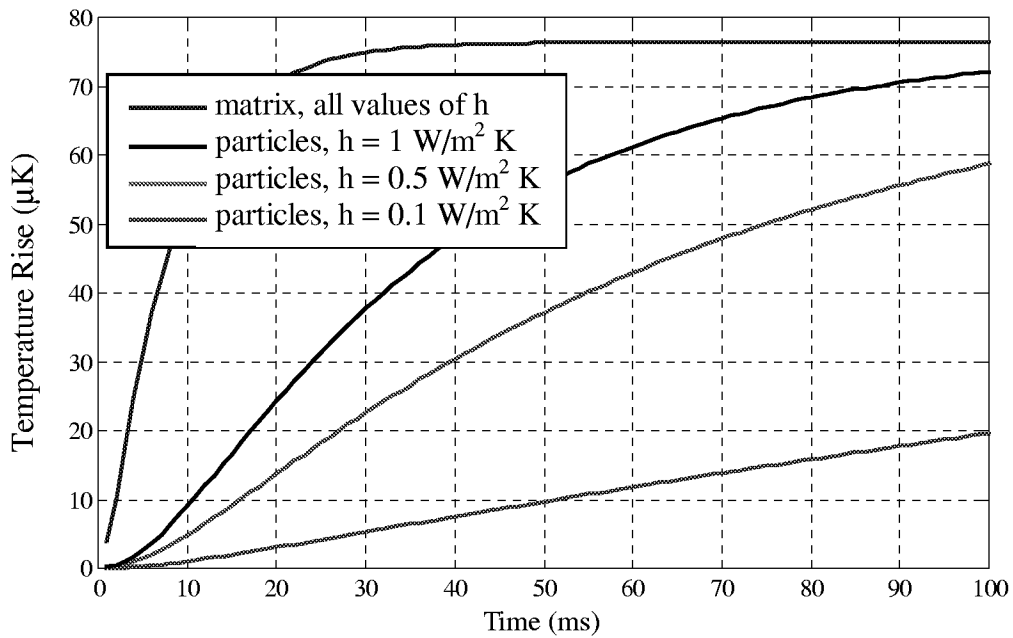


Figure 24: Matrix and particle temperatures at $x = 12 \mu\text{m}$ for different values of the contact conductance.

The effect of the particle size on the steady-state response of the detector is shown in Figure 25. The range of particle diameters was chosen so that the lumped capacity assumption holds. In this range it was found that the particle size has a very small effect

on the output of the detector. The maximum temperature change of the active junction is less than one-third of a percent.

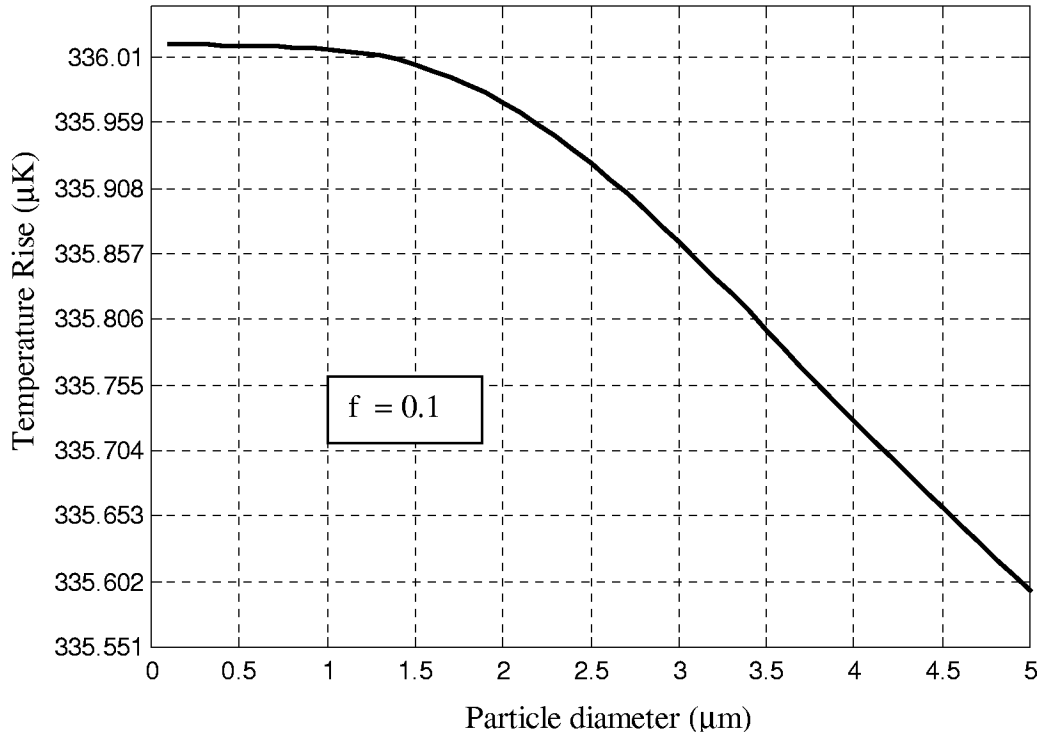


Figure 25: Particle size effect on the steady-state temperature rise of the active junction for a volume fraction of particles of ten percent.

4.1.3 Discussion of the results

The temperature response shown in the Figure 22 for the thermal radiation detector does not agree with what one would expect by doping a material of low thermal conductivity (the conductivity of the Parylene is $0.084 \text{ W/m}^2 \text{ K}$) with a material of higher thermal conductivity (the conductivity of the carbon particles is $1.59 \text{ W/m}^2 \text{ K}$). In Equation 4-1 of the two-step transient model, the conductivity K is equal to $(1 - f)k_m$, where k_m is the conductivity of the matrix. This expression for K requires that the thermal conductivity decrease as the volume fraction of particles increases, with the result that the temperature

of the active junction increases. With this model, the steady-state temperature distribution depends only on the thermal conductivity of the matrix and the volume fraction of particles, and not on the thermal conductivity of those particles. The steady-state temperature increases as the volume fraction of the particles increases. This is contrary to intuitive expectations as well as to observations of decreases in electrical resistance of Larc-Si layer with an increased loading of graphite particles [Sorensen, 1998].

It is hypothesized that this two-step model could be improved by somehow taking into account the thermal conductivity of the particles, even if the lumped capacity approximation is assumed. One way would be to solve the Laplace equation for heat conduction subject to the conditions of continuity of the temperature (assuming perfect contact between the particles and the matrix) and heat flux at the interface of each particle and the surrounding matrix. This direct method would of course be computationally intensive. The alternative approach in this thesis, described below, is to compute equivalent properties for a heterogeneous thermal impedance layer. The response of the detector is then analyzed using the analytical transient model developed in Chapter 2.

4.2 Heat transfer in a heterogeneous material using micromechanical property models.

4.2.1 Thermal analysis

The determination of the thermophysical properties of heterogeneous mixtures has been and continues to be a very active area of research because of the wide range of applications of these materials in engineering [Meredith et al., 1962]. Although some properties of these mixtures, such as the specific heat, do not present any difficulties, other thermal and transport properties, such as thermal or electrical conductivities, require more sophisticated treatments. The simple mixing rules that consist of averaging the transport properties of pure phases to get those of the mixture do not apply in these latter cases. The complexity of the problem increases for more concentrated mixtures.

The primary interest here is the determination of the effective thermal conductivity and heat capacity of a two-phase composite material consisting of spherical carbon particles embedded in a continuous matrix.

4.2.1.1 Effective thermal capacity of the mixture

The effective heat capacity of a mixture can be directly obtained using a simple mixing rule. The effective specific heat of the matrix-particle mixture is

$$\bar{c} = f'_p c_p + f'_m c_m \quad (4-5)$$

where subscripts p and m indicate “particle” and “matrix” respectively and f' is the appropriate mass fraction,

$$f'_i = \frac{m_i}{m_{mixture}} \quad (4-6)$$

Alternatively, we can define the volume fraction

$$f_i = \frac{V_i}{V_{mixture}} \quad (4-7)$$

with $i = p$ or m .

The relation between f'_i and f_i is $f'_i = \frac{\rho_i}{\bar{\rho}} f_i$, (4-8)

where $\bar{\rho}$ is the density of the mixture,

$$\bar{\rho} = \frac{\rho_p V_p + \rho_m V_m}{V_{mixture}} \quad (4-9)$$

Equation 4-5 is a statement of conservation of energy, and Equation 4-9 is a statement of conservation of mass.

Combining equations 4-5 and 4-6 yields

$$\overline{\rho c} = f(\rho c)_p + (1-f)(\rho c)_m \quad . \quad (4-10)$$

In Equation 4-10, $\overline{\rho c}$ is the effective heat capacity of the matrix-particle mixture and f is the volume fraction of the particles. Equation 4-10 is valid for both dilute and concentrated mixtures.

4.2.1.2 Effective thermal conductivity

The theoretical investigation of the equivalent thermal conductivity requires the distinction between dilute and concentrated mixtures.

4.2.1.2.1 Dilute mixtures

Dilute mixtures are mixtures in which the disturbance of the lines of heat flow by one particle is independent of the disturbance provoked by any other particle. For these dilute mixtures, Maxwell [1954] derived an equation for the effective electrical conductivity by solving the Laplace equation for a single sphere in a matrix. The mathematical behavior of the physical properties thermal and electrical conductivity being analogous, the result obtained for the effective electrical conductivity is applicable for the effective thermal conductivity.

The result obtained by Maxwell when the thermal conductivity is substituted for electrical conductivity, is

$$\overline{K} = \frac{K_d + 2 - 2f(1 - K_d)}{K_d + 2 + f(1 - K_d)} \quad , \quad (4-11)$$

where \bar{K} is the relative effective thermal conductivity that is the ratio of the effective thermal conductivity of the mixture, \bar{k} , to that of the matrix, k_m . The quantity K_d is the ratio of the thermal conductivity of the spherical particles, k_d , to that of the surrounding matrix.

Equation 4-11 is valid regardless of the size (particles of uniform size) and spatial distribution (random or ordered dispersions) of spherical particles as long as the volume fraction of the particles is less than 0.2 and the contact resistance between the particles and the matrix is negligible.

Hasselman and Johnson [1987] modified the theory of Maxwell and derived an expression for the effective thermal conductivity of mixtures with a thermal contact resistance between the particles and the matrix. They found that the effective thermal conductivity of a given composite system and dispersed phase do not depend only on the volume fraction of the particles but also on the particle size. They show that

$$\bar{K} = \frac{\left(K_d + \frac{2k_d}{ah} + 2\right) - 2f\left(1 - K_d + \frac{k_d}{ah}\right)}{\left(K_d + \frac{2k_d}{ah} + 2\right) + f\left(1 - K_d + \frac{k_d}{ah}\right)}, \quad (4-12)$$

where h is the contact conductance between the spherical particles and the matrix material, k_d is the thermal conductivity of the particles, and a is the diameter of the particles. Like the Maxwell expression, Equation 4-12 is valid only for dilute mixtures. When h goes to infinity Equation 4-12 reduces to Equation 4-11.

4.2.1.2.2 Concentrated mixtures

The determination of the effective properties of composites in which the volume fraction of the dispersed phase is high ($f > 0.2$) presents increased mathematical difficulties [Meredith et al., 1962]. As the volume fraction of particles increases, the heat flow fields

surrounding the particles begin to interact. The microstructure of the composite material begins to play a more important role and so does the manufacturing technique upon which the microstructure depends. The effective properties depend on the arrangement of the particles with respect to the direction of the heat flow lines. Many predictive formulas of the effective thermal conductivity have been derived for different geometries and arrangements of the dispersed phase. Lord Raleigh [1964] found that for a cubic array of spheres where the heat flow field is on the average perpendicular to a side of the cube, the effective thermal conductivity is given by

$$\bar{K} = 1 - \frac{3f}{(2 + K_d)/(1 - K_d) + f - 0.525(1 - K_d)f^{10/3} / (4/3 + K_d)} \quad (4-13)$$

Equation 4-13 is valid for f less than $\pi/6$. Meredith and Tobias [1962] derived another equation for \bar{K} for the same conditions using a different potential function. They found that

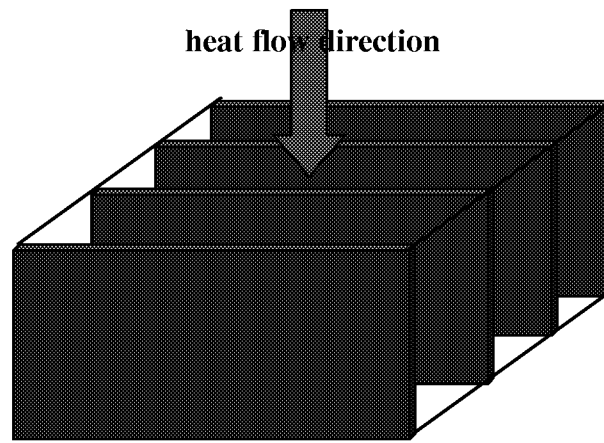
$$\bar{K} = 1 - \frac{3f}{(2 + K_d)/(1 - K_d) + f - 1.315(1 - K_d)f^{10/3} / [4/3 + K_d + 0.409(1 - K_d)f^{7/3}]} \quad (4-14)$$

Equations 4-13 and 4-14 are valid for the cases of ordered arrangements of the particles where the position of each particle is known and the locations of the particles are chosen so that they are symmetric and thus produce fewer interactions among particles. The general results for randomly distributed particles are quite different. A large number of relations exist in the literature for the computation of the effective thermal conductivity in the case of randomly distributed spherical particles in a matrix. The relation derived by Meredith and Tobias [1962] is used in the current investigation. For two-phase mixtures, Meredith and Tobias found that

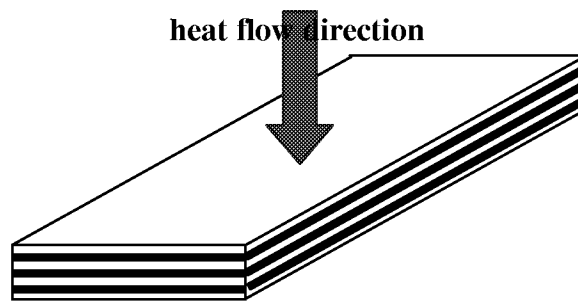
$$\bar{K} = \left[\frac{2(K_d + 2) + 2(K_d - 1)f}{2(K_d + 2) - (K_d - 1)f} \right] \left[\frac{(2 - f)(K_d + 2) + 2(K_d - 1)f}{(2 - f)(K_d + 2) - (K_d - 1)f} \right] \quad (4-15)$$

The maximum and minimum values of the thermal conductivity are obtained in the following limiting cases [McLachlan, 1990] :

- the particles of the suspended phase link up parallel to the direction of the mean heat flow, as in Figure 26 (a).
- the particles of the suspended phase link up perpendicular to the direction of the mean heat flow as in, Figure 26 (b).



(a)



(b)

Figure 26: (a) lamina parallel to the heat flow direction; (b) lamina perpendicular to the heat flow direction.

The effective thermal conductivities corresponding to these two cases are, respectively, the arithmetic mean and the harmonic mean of the thermal conductivity of the matrix and the particles. That is,

$$\bar{k} = fk_d + (1-f)k_m \quad (4-16)$$

and

$$1/\bar{k} = f/k_d + (1-f)/k_m \quad (4-17)$$

In Equations 4-16 and 4-17 \bar{k} is the effective thermal conductivity, k_d the thermal conductivity of the particles and k_m the thermal conductivity of the matrix. Note that Equations 4-16 and 4-17 follow directly from the limiting cases of the conductance of parallel and series networks, as shown in Figure 26.

4.2.1.3 Results

The effective thermal conductivity of dilute mixtures is governed by the magnitude of the parameter $k_d/(ah)$, as described by Equation 4-12. In a matrix doped with very small particles this term can have a strong influence on the effective thermal conductivity, as shown in Figure 27. The effective thermal conductivity is maximum when the contact between the matrix and the particles is perfect. The effective thermal conductivity is lowest when the nondimensional parameter $k_d/(ah)$ goes to infinity because of the additional thermal resistance to the heat transfer that builds around the particles. The determination of the contact resistance between the particles and the matrix would be a challenging experimental problem because of the dimensions of the detector. To obtain a first approximation of the effective thermal conductivity, the contact conductance term is neglected in this current effort and thus the Equations 4-11 and 4-15 are used in determining the effective thermal conductivities. The use of these two equations assumes randomly distributed particles in the matrix. The computer code *homog.cpp* listed in Appendix A has been modified to take into account the dependence of the heat capacity and the thermal conductivity of the thermal impedance layer on the volume fraction of the particles.

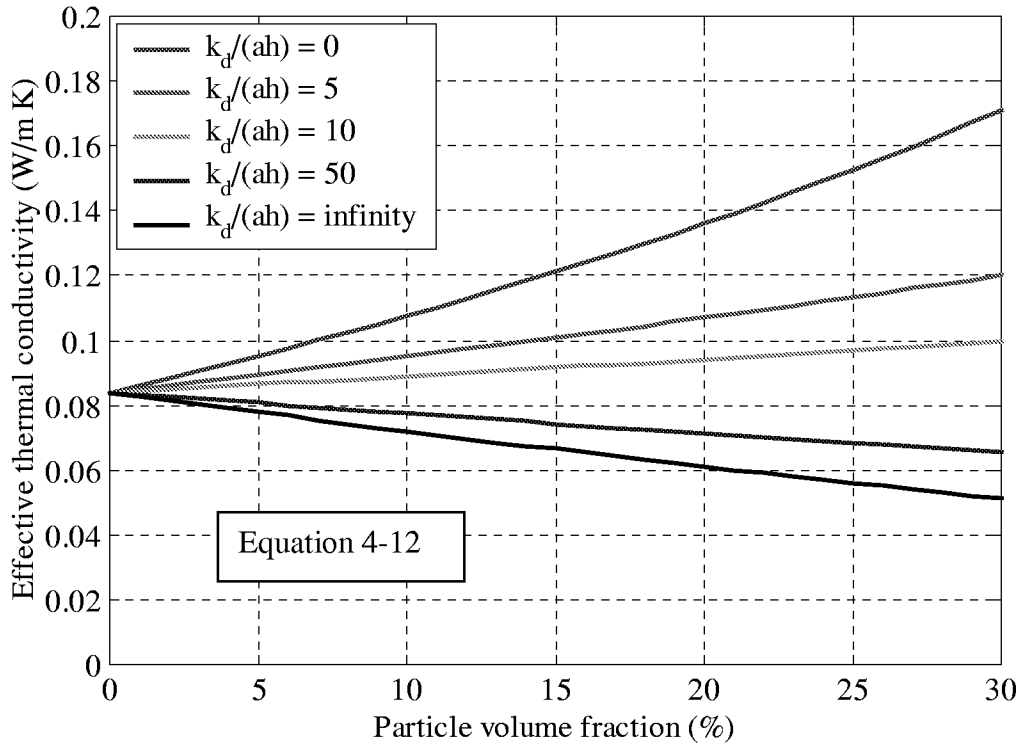


Figure 27: Effective thermal conductivity of the doped thermal impedance layer for $K_d = k_m/k_d = 18.93$ and for a range of k_d/ah .

The effective thermal conductivity of the thermal impedance layer is shown in Figure 28 for values of the particle volume fraction of up to fifty percent. An increase of the effective thermal conductivity of the matrix occurs as the volume fraction of the particles increases. Also presented in that figure are the two limiting cases, Equations 4-16 and 4-17. The effective thermal conductivity is bounded by these two limiting cases for the entire volume fraction range. It is clear that using one of these two limiting cases would lead to important errors in the value of the effective thermal conductivity, assuming the other models are correct. Equation 4-15 being in good agreement with the Maxwell expression, Equation 4-11, for a volume fraction less than twenty percent, it is used for computing the effective thermal conductivity for the entire range of values of the particle volume fraction.

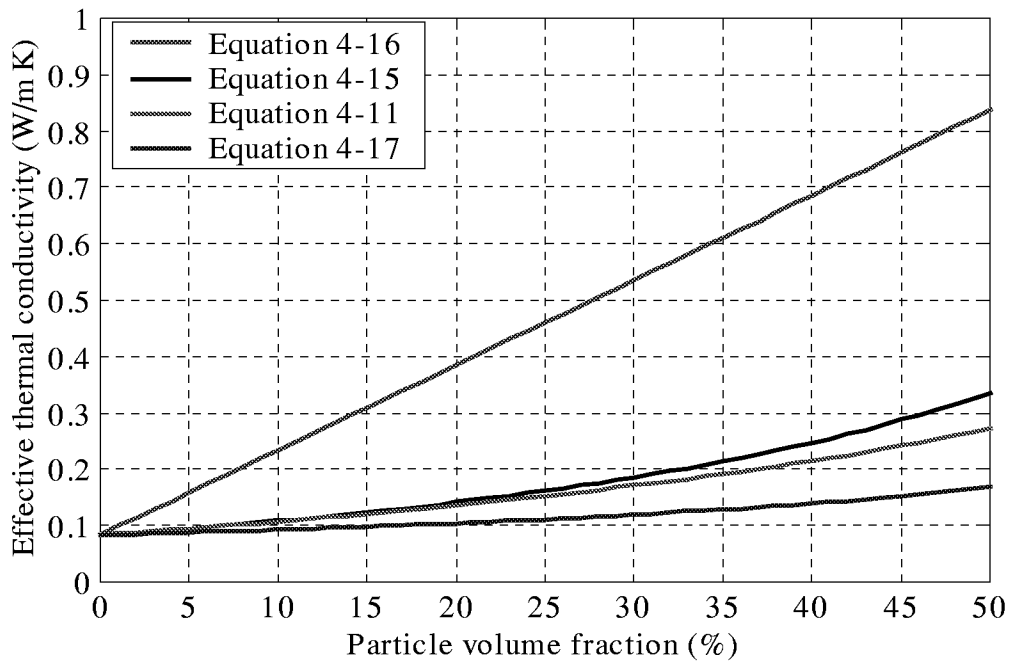


Figure 28: Prediction of the effective thermal conductivity of the doped impedance layer for $k_m = 0.084$ W/m K and $k_d = 1.59$ W/m K.

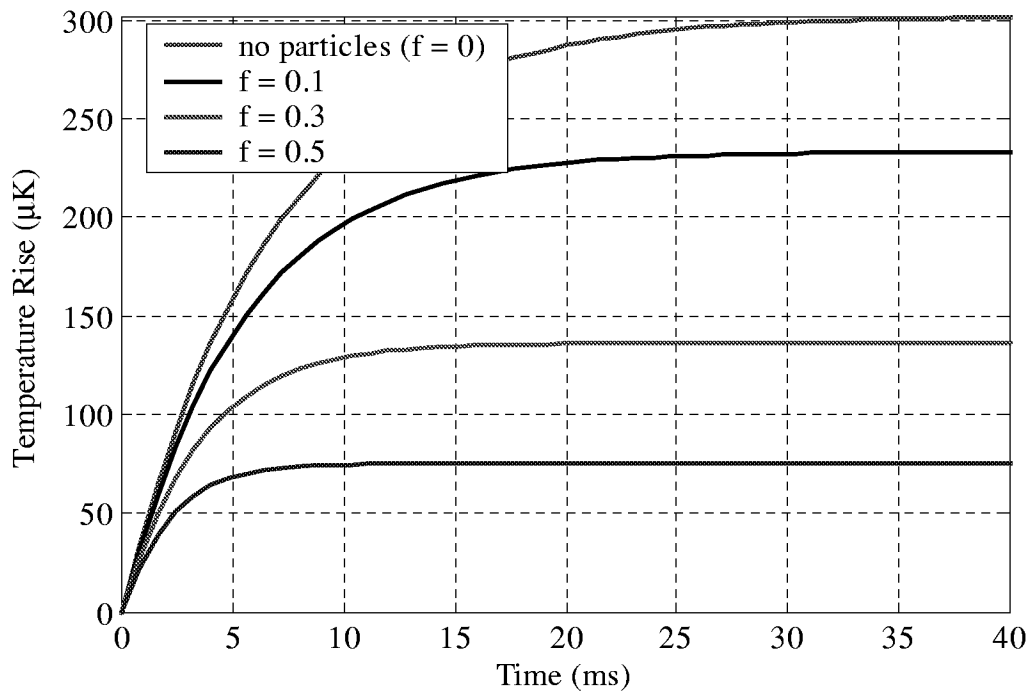


Figure 29: Active junction transient temperature rise of the detector with doped thermal impedance using homogeneous approximations method for a range of values of the volume fraction of the particles and $k_d/(ah) = 0$.

Figure 29 shows that the temperature of the active junction drops as the volume fraction of the particles increases, as expected. As the effective thermal conductivity of the impedance layer increases, more heat is transferred through the detector. The matrix being doped (perfect contact) with better thermally conducting particles, its ability to transfer heat to the layers below is improved. This is in keeping with the electrical conductivity experiments reported by Sorensen. Although the heat capacity of the matrix increases as the volume fraction of particles increases, Figure 29 shows a faster time response of the detector with increased particle volume fraction; that is the lower steady-state temperature is reached more quickly.

Figure 30 shows how the steady-state temperature of the active junction and the corresponding potential difference decrease when the particle volume fraction is increased. The temperature drops from about 300 to 75 μK and the potential difference from about 0.28 to 0.008 μV as the volume fraction goes from zero to 50 percent. The doping of the matrix by the particles greatly decreases the responsivity of the detector.

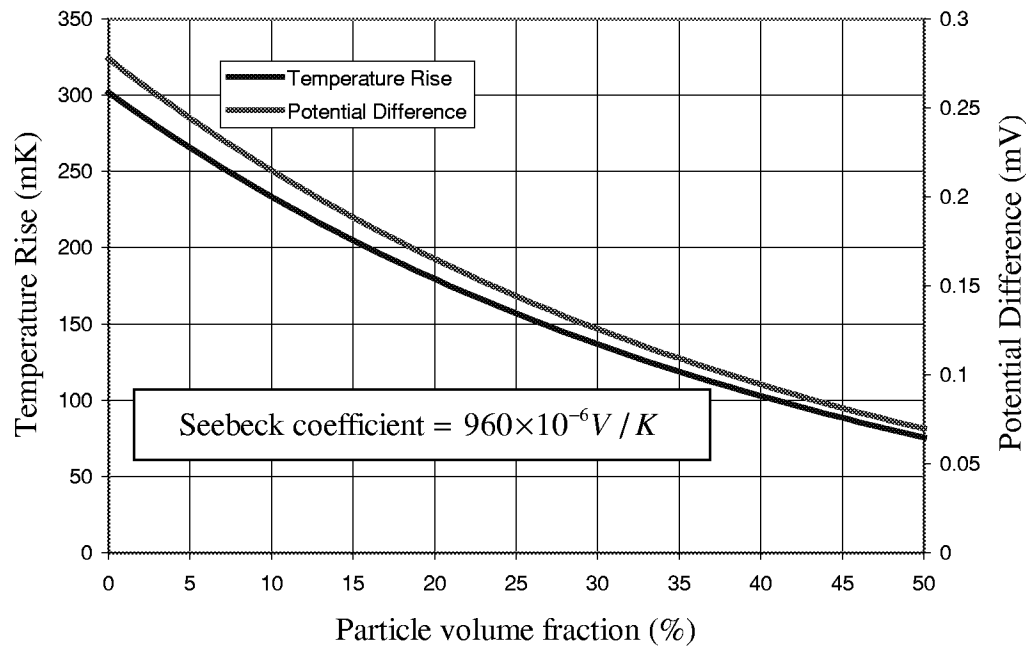


Figure 30: Active junction steady-state temperature rise and corresponding potential difference (Seebeck coefficient \times Temperature Rise) for a range of values of the volume fraction of the particles.

Finally the temperature distribution through the detector with the thermal impedance layer doped with fifty percent of particles is shown in Figure 31. The temperature gradients are smaller than those in Figure 4 but the temperatures of the two layers forming each junction are still essentially uniform through the junction. While the performance of the thermal impedance layer is diminished, the temperature of the reference junction remains that of the aluminum substrate. At this concentration of particles, the steady-state condition is reached in about ten milliseconds. That is, the time response of the doped detector is almost three times faster than that of the configuration without particles.

Figure 32 shows the steady-state temperature distribution through the detector computed using the two-step process model and the macromechanical model with thirty percent of particle volume fraction, and that of the undoped thermal detector. The contact conductance h is fixed high enough so that it can be assumed perfect contact between the matrix and the particles.

The use of the mixing rules for computing the effective thermal capacity and predictive formulas for the effective thermal conductivity of the matrix and particles gives results that are in accord with intuition. Although the predictive correlations start to break down for higher values of volume fraction, results given by the homogeneous approximations encompassed by Equations 4-10 and 4-15 are more realistic than those for the two-step model reported in Section 4-1.

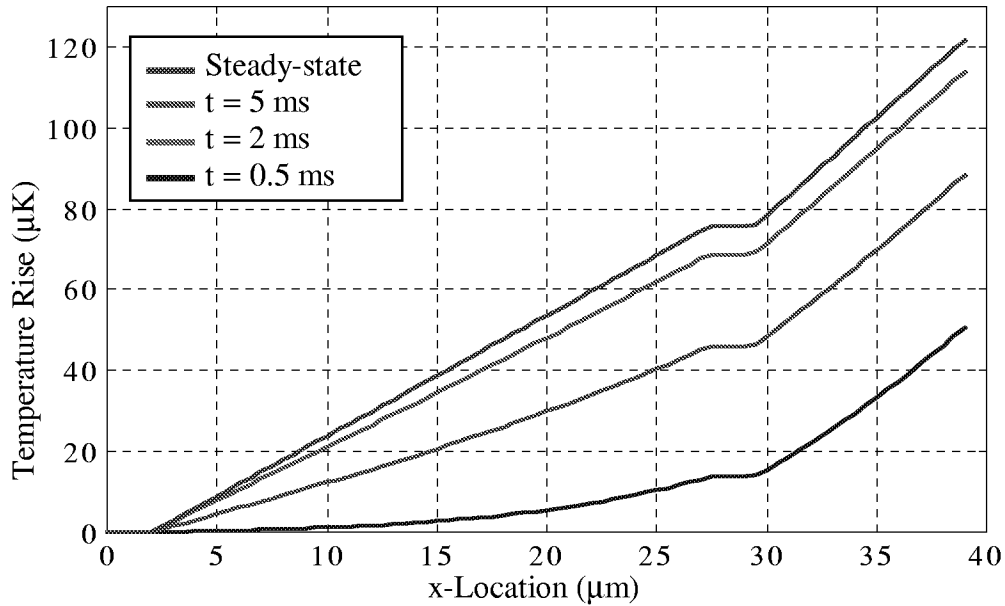


Figure 31: Temperature profile through the detector doped with fifty percent of carbon particles using the homogeneous approximations method to estimate the thermal conductivity and the heat capacity of the thermal impedance layer.

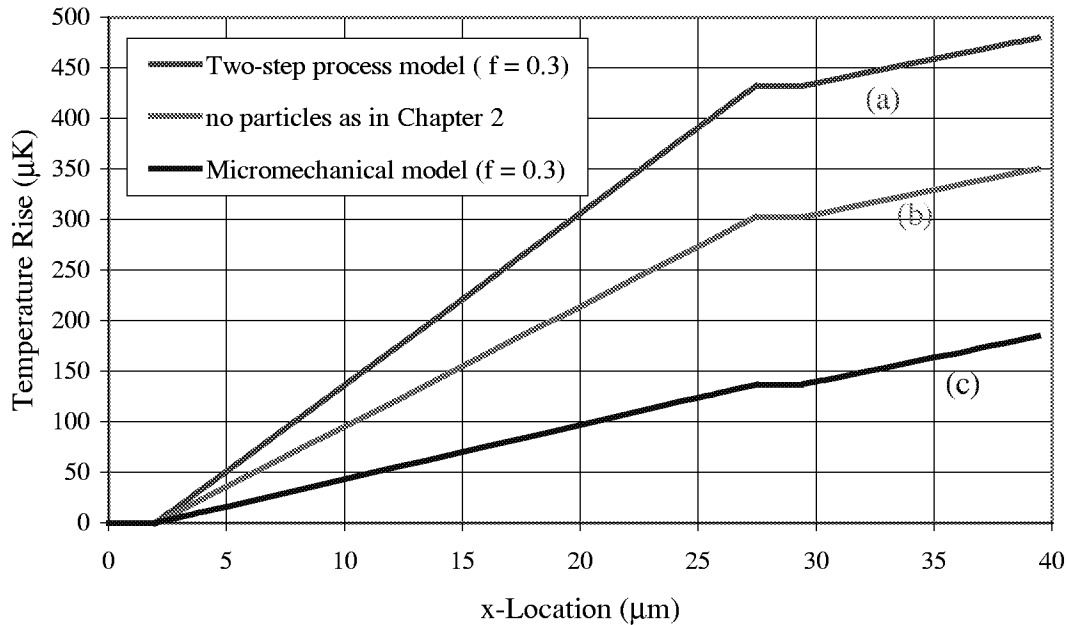


Figure 32: Comparison of steady-state temperature profile through the detector obtained using (a) the two-step model, with (c) that obtained using the micromechanical model, and (b) the undoped detector model (the thermal impedance layer of the detector is doped with thirty percent of particles for the first two cases).

4.2.2 Electrical analysis

4.2.2.1 Effective properties

The effective electrical conductivity of the system composed of a matrix doped with conductive particles is obtained using the same equations derived for the effective thermal conductivity (Equations 4-10 through 4-17). The objective is to determine how the effective electrical resistance between the upper surface (S_1) and the lower surface (S_2) of the thermal impedance layer, illustrated in Figure 33, changes as the volume fraction of the particles increases. The electric current flow is from S_1 to S_2 and the other two boundaries of the thermal impedance are assumed to be electrically insulated.

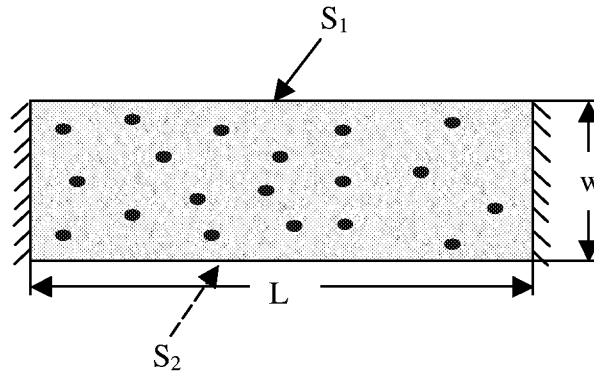


Figure 33: Thermal impedance layer doped with particles.

The heterogeneous matrix-particle system is electrically modeled as a homogenous material with effective electrical properties. Based upon the effective thermal conductivity equations, the relative effective electrical conductance is given by

$$\bar{\Lambda} = \left[\frac{2(\Lambda_d + 2) + 2(\Lambda_d - 1)f}{2(\Lambda_d + 2) - (\Lambda_d - 1)f} \right] \left[\frac{(2 - f)(\Lambda_d + 2) + 2(\Lambda_d - 1)f}{(2 - f)(\Lambda_d + 2) - (\Lambda_d - 1)f} \right], \quad (4-18)$$

where $\bar{\Lambda}$ is the relative effective electrical conductivity; that is, the ratio of the effective electrical conductivity of the mixture, $\bar{\sigma}$, to that of the matrix, σ_m , and the quantity Λ_d is the ratio of the electrical conductivity of the spherical particles, σ_d , to that of the surrounding matrix.

The electrical conductivity for the two limiting cases, i.e. Case (a) and (b) of Figure 26, is, respectively

$$\bar{\sigma} = f\sigma_d + (1-f)\sigma_m \quad (4-19)$$

and

$$1/\bar{\sigma} = f/\sigma_d + (1-f)/\sigma_m \quad . \quad (4-20)$$

The effective electrical resistance (\bar{R}) between the surfaces S_1 and S_2 of the thermal impedance layer is a function of the cross-sectional area S , the length L , and the effective resistivity ($\bar{\varphi} = \frac{1}{\bar{\sigma}}$) of that layer; that is,

$$\bar{R} = \bar{\varphi} \frac{w}{S} \quad . \quad (4-21)$$

4.2.2.2 Results and Discussions

The effective electrical resistance is determined using the homogeneous approximations for a Parylene layer with embedded carbon particles. The experimental determination of the electrical resistance actually underway at NASA Langley Research Center is done for a Larc-Si matrix with embedded carbon particles. The thermophysical properties of this new material being currently not well known, Parylene is considered in this investigation. However, the same equations could be used latter on when the properties of the Larc-Si are known.

The resistivities of Parylene and carbon are respectively 6×10^{14} and $7.27 \times 10^4 \Omega^{-1}m^{-1}$. The resistivity of Parylene being several orders of magnitude higher than that of the carbon, Equations 4-18 through 4-20 can be simplified and become respectively,

$$\bar{\sigma} = \bar{\Lambda} \times \sigma_m = \frac{(1+f)(2+f)}{(1-f)(2-f)} \times \sigma_m \quad , \quad (4-22)$$

$$\bar{\sigma} = f \sigma_d \quad , \quad (4-23)$$

and

$$\bar{\sigma} = \frac{\sigma_m}{1-f} \quad . \quad (4-24)$$

Figures 34 and 35 present the behavior of the effective resistivity and electrical resistance of the thermal impedance layer as the volume fraction of the particles increases. Although the figures show decreasing resistivity and electrical resistance, these two properties still remain far too high. The electrical conductivity of the Parylene is so low ($\sigma_m = 0.167 \times 10^{-14} \Omega^{-1}m^{-1}$) [Parylene Coating Services, 1999] that doping it with the carbon is not able to sufficiently improve the electrical properties of the thermal impedance. Another factor that influences the electrical resistance is the ratio w/S . This multiplying factor of the resistivity is equal to 7×10^3 for the dimensions of the thermal impedance (square cross-section with $L = 60 \mu m$ and $w = 25.4 \mu m$). The results show that doping the thermal impedance leads to a decrease in the electrical resistance. The decrease would be greater if the matrix had a much higher electrical conductivity to begin with.

The limiting cases, Equations 4-23 and 4-24, are not shown in Figure 31 because of their order of magnitude compare to that of Equation 4-22.

The approach presented here could be used to characterize the electrical performance of other combinations of matrices and particles, and different dimensions of the thermal impedance layer.

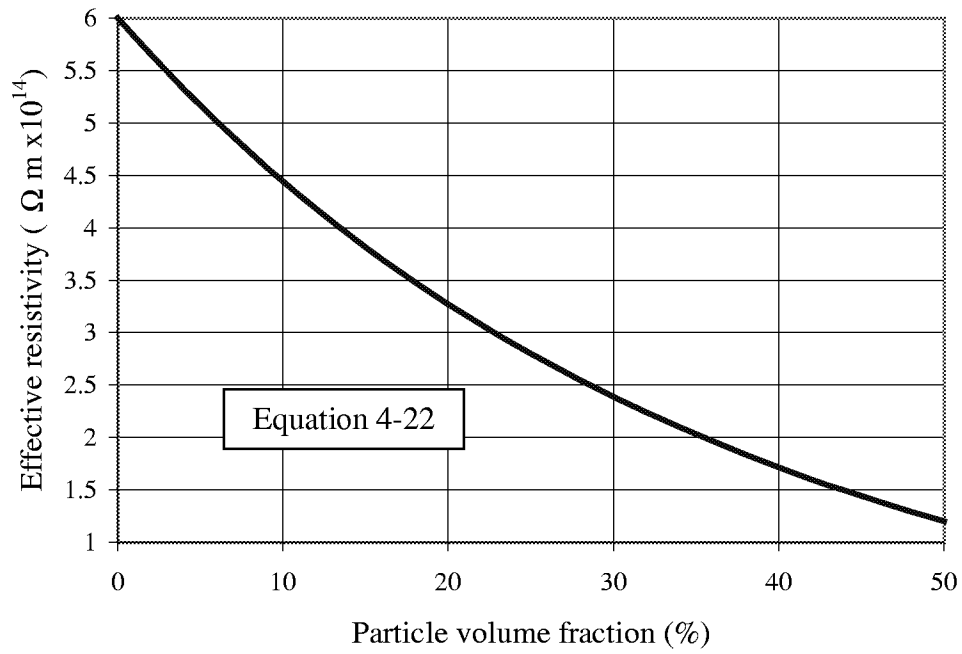


Figure 34: Effective resistivity of the thermal impedance layer defined by Figure 33 with $\sigma_m = 0.167 \times 10^{-14} \Omega^{-1} \text{ m}^{-1}$.

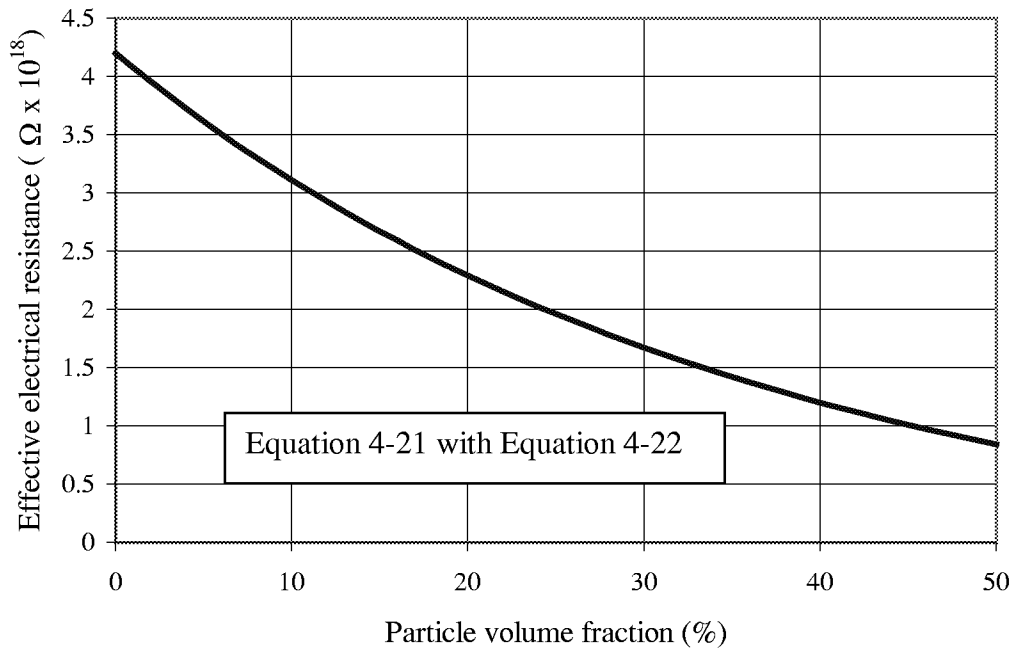


Figure 35: Effective electrical resistance of the thermal impedance layer defined by Figure 33 with $L = 25.4 \mu\text{m}$ and $S = 60 \times 60 \mu\text{m}^2$.

Chapter 5: Conclusions and Recommendations

5.1 Conclusions

Several results follow and conclusions can be drawn from the research reported in this thesis:

1. An analytical model based on the orthogonal expansion technique has been developed to characterize the effect on the performance of the thermal radiation detector of hypothetical contact resistance between the layers of detector.
2. The model shows that the existence of a contact resistance yields a greater temperature response of the detector. For example the steady-state temperature response of the detector rises from about 300 μK for a perfect contact between layers to 600 μK for an hypothetical 10,000 $\text{W/m}^2 \text{K}$ contact conductance between the layers.
3. The responsivity and time response of the detector both increase as the thickness of the thermal impedance layer increases. This suggests that an optimum configuration may exist within the constraints of geometry and input signal strength.
4. In order to investigate the possible effect of interface roughness on thermal conductivity, the random walk technique has been adapted for solving conduction heat transfer problems in two-dimensional geometries with specified boundary temperatures or insulated boundaries. The reproducibility

of the method is benchmarked by solving the special case of a one-dimensional heat conduction problem in a flat plate. Both the precision of the method and the machine time increase as the number of random walks increases.

5. The roughness effect model is unable to reproduce the decrease of the effective thermal conductivity of thin-films layers reported in the literature, and must be rejected as a possible explanation of the so-called thin-film effect.
6. A two-step model is used to characterize the heat conduction in the thermal impedance layer doped with conducting particles. The model predicts that by doping the thermal impedance layer with particles with higher thermal conductivity, the steady-state temperature response of the detector would increase, which is a counterintuitive.
7. The detector with doped thermal impedance layer performance is also investigated by determining effective electro- and thermophysical properties of the matrix-particle system using micromechanical models. Doping the thermal impedance layer of the matrix by conducting particles is shown to decrease the thermal impedance of the detector, as expected. As a result the detector responsivity decreases significantly. However the time response of the doped detector is found to be almost three times faster than that of the configuration without particles.
8. The decrease of the electrical resistance of the Parylene layer doped up to 50 percent by carbon particles does not have a significant effect on the electrical performance of the notional detector.
9. The thermal contact resistance and the micromechanical mixture models are expected to be useful in the ongoing parameter estimation activity in the Thermal Radiation Group.

5.2 Recommendations

Several recommendations can be drawn from the research reported in this thesis:

- 1 For further research in the development of the notional thin-film thermal radiation detector that is the subject of this effort, it is suggested that a special effort be dedicated to the determination of the unknown properties of the materials of the notional detector.
- 2 Although the current research was done using macroscale theories, the knowledge of properties such as the ratio of the thickness of a layer and the mean free path would give more insight in the understanding of the heat transfer process in the thermal radiation detector.
- 3 Measurement of the contact resistance between layers or the integration of its effect in an equivalent thermal resistance of layers will also be valuable.
- 4 Efforts should also be oriented toward the determination of other combinations of materials for the thermal impedance layer in order to decrease the electrical resistance of this layer without sacrificing its thermal performance.

References

Barreto, J., Experimental Design for estimating Electro-Thermophysical Properties of a Thermopile Thermal Radiation Detector, Master of Science Thesis, Mechanical Engineering Department, Virginia Polytechnic Institute and State University, Blacksburg, VA, USA, 1998.

Bejan, A., Advanced Engineering Thermodynamics, Wiley, New York, pp. 69-72, 1988.

Flik, M. I., B. I. Choi, and K. E. Goodson, "Heat Transfer Regimes in Microstructures," Journal of Heat Transfer, Vol. 114, pp. 666-674, 1992.

Flik, M. I., and C. L. Tien, "Size Effect on the Thermal Conductivity of Thin-Film Superconductors," ASME Journal of Heat Transfer, Vol. 112, pp. 872-881, 1990.

Haeffelin, M., Introduction to Atmospheric Science, ME 4984, Virginia Polytechnic Institute and State University, 1997.

Hasselman, D. P. H., and Lloyd F. Johnson, "Effective Thermal Conductivity of Composites with Interfacial Thermal Barrier Resistance," Journal of Composites Materials, Vol. 21, pp.508-515, 1987.

Hmina, N., and Y. Scudeller, "Thermal Interface Resistance and Subsurface Effusivity of Submicron Metallic Films on Dielectric Substrates: An Experimental Method For

Simultaneous Determination,” International Journal of Heat and Mass Transfer, Vol. 41, pp. 2781-2798.

Kelemen, F., “Pulse Method for the Measurement of the Thermal Conductivity of Thin-films,” Thin Solid Films, Vol. 36, pp. 199-203, 1976.

Kelkar, M., P. E. Phelan, and B. Gu, “Thermal Boundary Resistance for Thin-Film High T_c Superconductors at Varying Interfacial Temperature Drops,” International Journal of Heat Transfer, Vol. 40, pp. 2637-2645, 1997.

Kumar, S., and G. C. Vradis, “Thermal Conductivity of Thin Metallic Films,” Journal of Heat Transfer, Vol. 116, pp. 28-34, 1994.

Lambropoulos, J. C., M. R. Jolly, C. A. Amsden, S. E. Gilman, M. J. Sinicropi, D. Diakomihalis, and S. D. Jacobs, “Thermal Conductivity of Dielectric Thin-films,” Journal of Applied Physics, Vol. 66, pp.4230-4242, 1989.

Lee, S.-M., and D. G. Cahill, “Heat Transport in Thin Dielectric Films,” Journal of Applied Physics, Vol. 81, pp.2590-2595, 1997.

Lenoble, J., Atmospheric Radiative Transfer, A. Deepak Publishing, Hampton, VA, 1993.

Majumdar, A., “Microscale Heat Conduction in Dielectric Thin-films,” Journal of Heat Transfer, Vol. 115, pp.7-16, 1993

Maxwell, J. C., A Treatise on Electricity and Magnetism, 3rd Edition., Vol. 1, Dover Publications Inc., New York, N.Y, pp.435, 1954.

McLachlan, D. S., M. Blaszkiewicz and R. E. Newnham, “Electrical Resistivity of Composites,” J. Am. Ceram. Soc., Vol. 73, No 8, pp. 2187-2203, 1990.

Meredith, R. E., and C. W. Tobias, Conduction in Heterogeneous Systems, pp. 15-47 in Advances in Electrochemistry and Electrochemical Engineering, Vol. 2 Edited by C. W. Tobias, Interscience Publishers, New York, 1962.

Nath, P., and K. L. Chopra, “Thermal Conductivity of Copper Films,” Thin Solid films, Vol. 20, pp. 53-62, 1974.

Orain, S., Y. Scudeller, and T. Brousse, “Thermal Conductivity of ZrO₂ Thin-films,” Eurotherm Seminar n° 57, Microscale Heat Transfer, Poitiers, France, 1998.

Parylene Coating Services, Inc., Properties of dix dimmer, 1999.

Özsisik, M. N., Heat Conduction, 2nd Edition, John Wiley & Sons, New York, 1993.

Rayleigh, J. W. S., “ On the Influence of Obstacles Arranged in Rectangular Order upon the Properties of a Medium,” Scientific Papers by Lord Rayleigh, Vol. 4, Dover Publications Inc., New York, NY, pp. 19-38, 1964.

Sánchez, M. C., Optical Design of a Linear-Array Thermal Radiation Detector for Geostationary Earth Radiation Budget Application, Master of Science Thesis, Mechanical Engineering Department, Virginia Polytechnic Institute and State University, Blacksburg, VA, USA, 1998.

Shreider, Y. A., The Monte Carlo Method, Volume 87, Pergamon Press Ltd., 1966.

Smith, A. M., Prediction and Measurement of Thermal Exchanges within Pyranometers, Master of Science Thesis, Mechanical Engineering Department, Virginia Polytechnic Institute and State University, Blacksburg, VA, USA, 1999.

Sorensen, I. J., Analytical and Experimental Characterization of a Linear-Array Thermopile Scanning Radiometer for Geo-Synchronous Earth Radiation Budget

Applications, Master of Science Thesis, Mechanical Engineering Department, Virginia Polytechnic Institute and State University, Blacksburg, VA, USA, 1998.

Tzou, D.Y., Macro- to Microscale Heat Transfer: The Lagging Behavior, Taylor & Francis, 1997.

Vick, B., Conduction Heat Transfer, ME 5304, Virginia Polytechnic Institute and State University, VA, USA, 1998.

Vick, B., and E. P. Scott, "Heat Transfer in a Matrix with Embedded Particles," Proceedings of the 1998 IMECE, Anaheim, CA, November 15-20, Vol.4, pp. 193-198.

Weckmann, S., Dynamic Electrothermal Model of a Sputtered Thermopile Thermal Radiation Detector for Earth Radiation Budget Applications, Master of Science Thesis, Mechanical Engineering Department, Virginia Polytechnic Institute and State University, Blacksburg, VA, USA, 1997.

Zima, J. M., Electrons and Phonons, Oxford University Press, London, United Kingdom, 1960.

Appendix A: homog.cpp

The program *homog.cpp* computes the temperature rise above the aluminum substrate within the thermal radiation at a given location, x , and a given time, t .

List of functions

* *eigen*

The function *eigen* returns the determinant of the matrix in Equation 2-47.

* *zbrak*

This function is used by the bisection method for root finding. When a function has multiple roots in an interval, *zbrak* determines the subintervals in that interval containing just one root.

* *findroot*

findroot is a root finder by bisection method. This function is used to determine the eigenvalues by setting the determinant returned by the function *eigen* equal to zero.

* *cprime*

cprime computes $\sum\{x_node[j-1]*(1/K[j-1]-1/K[j])\}$ for $j = 1: i$.

* *Nm*

Nm is the normalization integral.

* *Cm*

Cm returns the coefficients of $\theta_{i,i}$.

List of variables

<i>A</i>	matrix in Equation 2-47
<i>A[]</i> and <i>B[]</i>	vectors of the coefficients of the $X_{i,m}$'s
<i>alpha []</i>	thermal diffusivity vector, m^2/s


```

A(1,1)=sin(guess_beta*rap[1]);
A(1,2)=-sin(guess_beta*rap[2]*x_node[1]/x_node[2]);
A(1,3)=-cos(guess_beta*rap[2]*x_node[1]/x_node[2]);
A(2,1)=kij[1]*cos(guess_beta*rap[1]);
A(2,2)=-cos(guess_beta*rap[2]*x_node[1]/x_node[2]);
A(2,3)=sin(guess_beta*rap[2]*x_node[1]/x_node[2]);
A(3,2)=sin(guess_beta*rap[2]);
A(3,3)=cos(guess_beta*rap[2]);
A(3,4)=-sin(guess_beta*rap[3]*x_node[2]/x_node[3]);
A(3,5)=-cos(guess_beta*rap[3]*x_node[2]/x_node[3]);
A(4,2)=kij[2]*cos(guess_beta*rap[2]);
A(4,3)=-kij[2]*sin(guess_beta*rap[2]);
A(4,4)=-cos(guess_beta*rap[3]*x_node[2]/x_node[3]);
A(4,5)=sin(guess_beta*rap[3]*x_node[2]/x_node[3]);
A(5,4)=sin(guess_beta*rap[3]);
A(5,5)=cos(guess_beta*rap[3]);
A(5,6)=-sin(guess_beta*rap[4]*x_node[3]/x_node[4]);
A(5,7)=-cos(guess_beta*rap[4]*x_node[3]/x_node[4]);
A(6,4)=kij[3]*cos(guess_beta*rap[3]);
A(6,5)=-kij[3]*sin(guess_beta*rap[3]);
A(6,6)=-cos(guess_beta*rap[4]*x_node[3]/x_node[4]);
A(6,7)=sin(guess_beta*rap[4]*x_node[3]/x_node[4]);
A(7,6)=sin(guess_beta*rap[4]);
A(7,7)=cos(guess_beta*rap[4]);
A(7,8)=-sin(guess_beta*rap[5]*x_node[4]/x_node[5]);
A(7,9)=-cos(guess_beta*rap[5]*x_node[4]/x_node[5]);
A(8,6)=kij[4]*cos(guess_beta*rap[4]);
A(8,7)=-kij[4]*sin(guess_beta*rap[4]);
A(8,8)=-cos(guess_beta*rap[5]*x_node[4]/x_node[5]);
A(8,9)=sin(guess_beta*rap[5]*x_node[4]/x_node[5]);
A(9,8)=sin(guess_beta*rap[5]);
A(9,9)=cos(guess_beta*rap[5]);
A(9,10)=-sin(guess_beta*rap[6]*x_node[5]/x_node[6]);
A(9,11)=-cos(guess_beta*rap[6]*x_node[5]/x_node[6]);
A(10,8)=kij[5]*cos(guess_beta*rap[5]);
A(10,9)=-kij[5]*sin(guess_beta*rap[5]);
A(10,10)=-cos(guess_beta*rap[6]*x_node[5]/x_node[6]);
A(10,11)=sin(guess_beta*rap[6]*x_node[5]/x_node[6]);
A(11,10)=cos(guess_beta*rap[6]);
A(11,11)=-sin(guess_beta*rap[6]);

return A.LogDeterminant().Value(); //computes the determinant
}

//-----

```

```

void zbrak(float (*fx)(float x,float rap[],float x_node[],float kij[]),float x1,float x2,int n ,float
xb1[], float xb2[], int *nb,float rap[],float x_node[],float kij[])
{
    int nbb=0,i;
    float x,fp,fc,dx;
    x=x1;
    dx=(x2-x1)/n;
    fp=(*fx)(x1,rap,x_node,kij);

    for (i=1;i<=n;i++)
    {
        fc=(*fx)(x+=dx,rap,x_node,kij);
        if (fp*fc<=0.0)
            {
                xb1[++nbb]=x-dx;
                xb2[nbb]=x;
                if (*nb==nbb)return;
            }
        fp=fc;
    }
    *nb=nbb;
}

```

//-----

```

void find_root (float (*fx)(float x,float rap[],float x_node[],float kij[]),float xb1[],float xb2[], float
beta[],int nb,float rap[],float x_node[],float kij[])
{
    for (int i=1;i<=nb;i++)
    {
        float x1=xb1[i];
        float x2=xb2[i];
        float x_mid, estimated_root;
        float precision_x = pow(10,-5);
        int number_iteration=0,max_iteration=50;

        if (fabs((*fx)(x1,rap,x_node,kij))<=precision_x)
            estimated_root=x1;

        else if (fabs((*fx)(x2,rap,x_node,kij))<=precision_x)
            estimated_root=x2;

        else if ((*fx)(x1,rap,x_node,kij)*(*fx)(x2,rap,x_node,kij)>0)
            {
                cout<<"There's no root between x1 and x2.\n";
            }
    }
}

```

```

        exit(EXIT_FAILURE);
    }

    else if ((*fx)(x1,rap,x_node,kij)*(*fx)(x2,rap,x_node,kij)<0)
    {
        do
        {
            x_mid=0.5*(x1+x2);

            if ((*fx)(x_mid,rap,x_node,kij)==0)
                estimated_root=x_mid;

            else if ((*fx)(x1,rap,x_node,kij)*(*fx)(x_mid,rap,x_node,kij)<0)
                x2=x_mid;
            else
                x1=x_mid;

            number_iteration+=1;
        }
        while (number_iteration<=max_iteration&fabs(0.5*(x2-
x1))>precision_x&fabs((*fx)(x_mid,rap,x_node,kij))>precision_x);
        estimated_root=x_mid;
    }

    beta[i]=estimated_root;
}
}

```

//-----

```

float cprime(int i,float x_node[], float K[])
{
    float result=0.0;
    if (i==1)
        return 0;
    else
        { for (int j=2;j<=i;j++)
            result+=x_node[j-1]*(1/K[j-1]-1/K[j]);}
    return result;
}

```

//-----

```

float Nm(float A[],float B[],float K[],float x_node[],float alpha[],float b)
{
    float sum_1=0.0;

```



```

for(int i=1;i<=6;i++)
{
float u=2*x_node[i-1]*b/sqrt(alpha[i]);
float v=2*x_node[i]*b/sqrt(alpha[i]);
sum_1+=K[i]/alpha[i]*(0.5*(A[i]*A[i]+B[i]*B[i])*(x_node[i]-x_node[i-1])+
0.5/b*A[i]*B[i]*sqrt(alpha[i])*(cos(u)-cos(v))+
sqrt(alpha[i])/(4.0*b)*(A[i]*A[i]-B[i]*B[i])*(sin(u)-sin(v))));
}
return sum_1;
}
//-----

float Cm(float A[],float B[],float K[],float x_node [],float alpha[],float b,float q)
{
float sum_2=0.0;
for (int i=1;i<=6;i++)
{
float u=x_node[i-1]*b/sqrt(alpha[i]);
float v=x_node[i]*b/sqrt(alpha[i]);
sum_2+=-q/(sqrt(alpha[i])*b*b)*((A[i]*cprime(i,x_node,K)*K[i]*b-B[i]*sqrt(alpha[i]))*
(cos(u)-cos(v))-(A[i]*sqrt(alpha[i])+B[i]*cprime(i,x_node,K)*K[i]*b)*
(sin(u)-sin(v))+A[i]*b*(x_node[i-1]*cos(u)-x_node[i]*cos(v))-
B[i]*b*(x_node[i-1]*sin(u)-x_node[i]*sin(v)));
}

return (sum_2/Nn(A,B,K,x_node,alpha,b));
}
//-----

// Beginning of the main program

int main()
{
// Initialization
float t=0.02;//time (ms)
float x=39.4*pow(10,-6);//location in the detector
float q=1.0;//heat flux q=1W/m2.K
float K[7]={0,71.6,60,0.084,71.6,60,0.209};//layers conductivity (W/m.K)
float Thickness[7]={0,coef,coef,25.4*coef,coef,coef,10*coef};//layers thickness (m)
float Specific_heat[7]={0,133.0,200.0,712.0,133.0,200.0,669.0};//specific heat(J/kg.K)
float Mass_density[7]={0,21450.0,6880.0,1289.0,21450.0,6880.0,1400.0};//(kg/m^3)
float t_trans=0;//initialization of the transient temperature
float phi;
int layer;// index of layer

```

```

float alpha[7]={0}; //layers diffusivity (m^2/s)
float rap[7]={0}; //rap gives the ratio x_node[i]/sqrt(alpha[i]) for computing eta[i]
float x_node[7]={0.0};
    for (int i=1;i<7;i++)
        {
            x_node[i]=x_node[i-1]+Thickness[i];
            alpha[i]=K[i]/(Mass_density[i]*Specific_heat[i]);
            rap[i]=x_node[i]/sqrt(alpha[i]);
        }

float kij[6]={0}; //kij gives the value of (K[i]/K[i+1])*sqrt(alpha[i+1]/alpha[i])
    for (i=1;i<6;i++)
        {
            kij[i]=(K[i]/K[i+1])*sqrt(alpha[i+1]/alpha[i]);
        }
int nb=10; //nb is the maximum of eigenvalues sought
float beta[11]={0};
float xb1[11]; //size always nb+1
float xb2[11]; //size always nb+1
zbrak(eigen,0.0,290.0,10,xb1,xb2,&nb,rap,x_node,kij);

find_root (eigen,xb1,xb2,beta,nb,rap,x_node,kij); //computes the eigenvalues

//find the layer index corresponding to the value of x

    if (x>0.0 && x<=coef)
        layer=1;

    else if (x>coef && x<=2*coef)
        layer=2;

    else if (x>2*coef && x<=27.4*coef)
        layer=3;

    else if (x>27.4*coef && x<=28.4*coef)
        layer=4;

    else if (x>28.4*coef && x<=29.4*coef)
        layer=5;
    else
        layer=6;

for (int indbeta=1;indbeta<=nb;indbeta++)
    {
        float b=beta[indbeta];

```

```

float A[7]={0.0,1.0};
float B[7]={0.0,0.0};

for (i=1;i<=5;i++)
{
    float eta=rap[i]*b;
    float c=x_node[i]*rap[i+1]*b/x_node[i+1];

    A[i+1]=sin(c)*(A[i]*sin(eta)+B[i]*cos(eta))+kij[i]*cos(c)*(A[i]*cos(eta)-B[i]*sin(eta));
    B[i+1]=cos(c)*(A[i]*sin(eta)+B[i]*cos(eta))-kij[i]*sin(c)*(A[i]*cos(eta)-B[i]*sin(eta));

}

phi=A[layer]*sin(b*x/sqrt(alpha[layer]))+B[layer]*cos(b*x/sqrt(alpha[layer]));
t_trans+=exp(-b*b*t)*Cn(A,B,K,x_node,alpha,b,q)*phi;//computes the transient component
of the temperature rise.

}

float t_ss=q*(x/K[layer]+cprime(layer,x_node,K)); //steady-state component.

//displays on the screen the values of the location, time, and temperature rise
cout<<"\nThe temperature rise at x = "<<x<<" at t="<<t<<" is"<<(t_trans+t_ss)*pow(10,6)
<<" _micro_K"<<"\n\n";

return 0;
}

```

Appendix B: randwalk2d.cpp

```
*****  
The computer program randwalk2d.cpp determines the temperature at a given location using a two-  
dimensional random walk algorithm. The boundary conditions are specified temperature at the  
upper and lower surfaces, and insulated at the two other surfaces.  
*****
```

```
// C++ headers
```

```
#include<iostream.h>  
#include<math.h>  
#include<stdlib.h>  
#include<stdio.h>  
#include<time.h>  
#include<fstream.h>  
//-----
```

List of variables

N number of random walks
 n_x number of nodes in the x direction
 n_y number of nodes in the y direction
 L dimension in the x direction, m
 H dimension in the y direction, m
 dx step size in the x direction, m
 dy step size in the y direction, m
 r random number
 (x_i, y_i) coordinates of the starting point, m
 T_1 temperature of the upper surface, K

T_2 temperature of the lower surface, K

ofstream Point5_file("result.dat");//create a file called result to store the temperature distribution.

```
float funct_1(float x,float H) //the upper and lower boundary
{ return 0*sin(3*x)+0.5; } // of the surface are represented by
float funct_2(float x,float H) // trigonometric functions
{ return 0.0*cos(x)-0.5; }
```

// start of the main program

```
int main()
{
```

//Initialization

```
clock_t start_time=clock();
int N=1500; // number of simulations at each node.
int nx=100;// number of discrete points in the x-direction
float L=10.0;//dimension in the x direction, m
float H=1; //dimension in the y direction, y
int ny=100;// number of discrete points in the y-direction
float dx=L/nx;//step size in the x-direction
float dy=H/ny;//step size in the x-direction
float r;//random number;
float xi=dx/2.0;//x coordinate
float yi=dy/2.0;//y coordinate
float T_1=20;//temperature of the upper surface
float T_2=0;//temperature of the lower surface
float temp=0.0;
```

//change the seed of the random number generator

```
int seed=(int) time(NULL);
srand(seed);
```

```
for (int i=1;i<=N;i++)
```

```
{
```

```
float x=xi;
```

```
float y=yi;
```

```
while (y<funct_1(x,H) && y>funct_2(x,H))
```

```
{
```

```
if(x == )
```

```

    {
        x+=dx/2;
        y=y;
    }

    if(x == L)

        {
            x-=dx/2;
            y=y;
        }

    r=rand()/(RAND_MAX+1.0); // drawing of the random number

// search for direction

    if (r<0.25)
    {
        y=y;
        if (x == dx/2)
            x- = dx/2;
        else
            x- = dx;
    }

    else if(r>=.25 && r<0.5)
    {
        y = y;
        if (x == L-dx/2.0)
            x+ = dx/2;
        else
            x+ = dx;
    }

    else if (r>=0.5 && r<0.75)

        {
            x=x;
            y-=dy;
        }

    else
    {
        x = x;

```

```

        };          y+=dy;
    };
}

// temperature computation after a boundary node is reached

    if (y>0)
        temp+=T_1;
    else

        temp+=T_2;

}

//write in the file result
Point5_file<<xi<<" "<<yj<<" "<<temp/N<<"\n";

//compute the machine time

clock_t stop_time=clock();
cout<<"Time taken = "<<(stop_time-start_time)/CLOCKS_PER_SEC<<" secs.\n";

return 0;

}

```

Appendix C: eff_cond.cpp

```
*****  
This code uses a finite difference scheme to determine the temperature profile in a two-dimensional  
geometry. The temperature distribution obtained is used to approximate the heat flux in the y  
direction for the geometry in Figure 19. Equation 3-15 is then used to compute the ratio of the  
effective and bulk conductivities.  
*****
```

```
//C++ headers
```

```
#include<iostream.h>  
#include<math.h>  
#include<stdio.h>  
#include<fstream.h>
```

```
//creation of different files
```

```
ofstream Point1_file("fd2d.dat"); //temperature file  
ofstream Point2_file("x.dat"); //x coordinate  
ofstream Point3_file("y.dat"); //y coordinate  
ofstream Point4_file("h_ratio.dat"); //ratio R/(R+H) and k_eff/k_bulk
```

```
const int ii=5;//number of control volumes in the x_direction  
const int kk=20;//number of control volume by which R has been divided
```

```
//The function convergence checks if the convergence criteria during the computation of the  
// temperature is satisfied
```



```

float convergence (float (*M_1)[ii+3],float (*M_2)[ii+3],int jj)
{
    float sum=0.0;

    float (*M)[ii+3]=new float [jj+kk+3][ii+3];

    for(int j=1;j<=jj+kk+2;j++)

        for (int i=1;i<=ii+2;i++)

            {
                M[j][i]=M_2[j][i]-M_1[j][i];

                sum+=M[j][i];
            }

    return fabs(sum)/((jj+kk)*ii);
}

//beginning of the main program

int main()
{

//Initialization

int jj=1; //number of control volumes in the y direction
float (*Tj)[ii+3]=new float [jj+kk+3][ii+3];
float L=0.5;//length of the surface
float R=0.08;// height of the roughness
float H_ini=0.1;
float H=H_ini;//initial value of H
float k_bulk=405.46;//bulk conductivity (W/m.K)
float x[ii+3]={0};
float y_step=H_ini/4;//constant step size in the y-direction.

//the step size being constant in the y-direction, when R increases
//the number of control volume jj increases also. This keeps the size of the control volumes
//constant

for( int step=1;step<=10;step++)// this loop set the number of values of H
{
    //that will be considered, R being constant.

H+=0.2; //increment of H
jj=H/y_step; //new number of control volumes in the y-direction
float total_heat=0.0; //initial value of the total heat flux

```

```

float (*k)[ii+3]=new float [jj+kk+3][ii+3]; //thermal conductivity matrix

for (int j=1;j<=jj+1;j++)
    for (int i=1;i<=ii+2;i++)
        k[j][i]=k_bulk;

for (j=jj+2;j<=jj+kk+2;j++)
    for (int i=1;i<=ii+2;i++)
    {
        if (i%2==0) // specifying this high value for the thermal conductivity
            k[j][i]=pow(10,19); // sets the temperature of those control volumes equals
        else // to the surface temperature and models the geometry in Figure 18.
            k[j][i]=k_bulk; // the remaining control volumes are assigned the bulk conductivity.
    }

float dx[ii+3]={0};
for (int i=2;i<=ii+1;i++) //step size in the x-direction
    dx[i]=L/ii;

float *dy=new float [jj+kk+3]; //initialization of the step size in the y direction
dy[0]=0, dy[1]=0, dy[jj+kk+3]=0;

for ( j=2;j<=jj+1;j++)
    dy[j]=H/jj;

for ( j=jj+2;j<=jj+kk+1;j++)
    dy[j]=R/kk;

-----
//creation vectors of the coordinates of the control volumes
//x_coordinates
    for (i=2;i<=ii+2;i++)
        x[i]=x[i-1]+0.5*(dx[i-1]+dx[i]);

//y_coordinates
    float (*y)=new float[jj+kk+3];
    for (j=1;j<=jj+kk+2;j++)
        y[j]=y[j-1]+0.5*(dy[j-1]+dy[j]);

//-----
//Initialization of the matrices
//These matrices are defined by Vick [1998].

```

```

float (*aE)[ii+3]=new float[jj+kk+3][ii+3];
float (*aW)[ii+3]=new float[jj+kk+3][ii+3];
float (*aN)[ii+3]=new float[jj+kk+3][ii+3];
float (*aS)[ii+3]=new float[jj+kk+3][ii+3];
float (*a)[ii+3]=new float[jj+kk+3][ii+3];
float (*b)[ii+3]=new float[jj+kk+3][ii+3];
float (*p)[ii+3]=new float[jj+kk+3][ii+3];
float (*q)[ii+3]=new float[jj+kk+3][ii+3];
//-----
//Boundary conditions

// at x=0                //insulated
for(j=1;j<=jj+kk+2;j++)
{
  aE[j][1]=2*k[j][2]/dx[2];
  a[j][1]=aE[j][1];
  b[j][1]=0;
}

// at x=L                //insulated
for(j=1;j<=jj+kk+2;j++)
{
  aW[j][ii+2]=2*k[j][ii+1]/dx[ii+1];
  a[j][ii+2]=aW[j][ii+2];
  b[j][ii+2]=0.0;
}

// at y=0                //specified temperature
for(i=1;i<=ii+2;i++)
{
  aN[1][i]=0;
  a[1][i]=1;
  b[1][i]=0.0;                //temperature specified is 0
}

// at y=H                //specified temperature
for(i=1;i<=ii+2;i++)
{
  aS[jj+kk+2][i]=0;
  a[jj+kk+2][i]=1;
}

```

```

b[jj+kk+2][i]=100;          //specified temperature 100 K
}
//-----
// Computation of the different coefficients aE,aN,aW,aO,a,b

for (i=2;i<=ii+1;i++)
{
    for(j=2;j<=jj+kk+1;j++)
    {
        aW[j][i]=2*k[j][i-1]*k[j][i]*dy[j]/(dx[i-1]*k[j][i]+dx[i]*k[j][i-1]);
        aE[j][i]=2*k[j][i]*k[j][i+1]*dy[j]/(dx[i]*k[j][i+1]+dx[i+1]*k[j][i]);
        aS[j][i]=2*k[j-1][i]*k[j][i]*dx[i]/(dy[j-1]*k[j][i]+dy[j]*k[j-1][i]);
        aN[j][i]=2*k[j][i]*k[j+1][i]*dx[i]/(dy[j]*k[j+1][i]+dy[j+1]*k[j][i]);
        b[j][i]=0;//no source term
        a[j][i]=aW[j][i]+aE[j][i]+aS[j][i]+aN[j][i];
    }
}

//-----

//initialization of the temperature at all the nodes

float (*T_guess)[ii+3]=new float[jj+kk+3][ii+3];

for(j=1;j<=jj+kk+2;j++)
    for (int i=1;i<=ii+2;i++)
        T_guess[j][i]=0.0;

float (*T)[ii+3]=new float[jj+kk+3][ii+3];

for(j=1;j<=jj+kk+2;j++)
    for (int i=1;i<=ii+2;i++)
        T[j][i]=T_guess[j][i];

float (*Ti)[ii+3]=new float[jj+kk+3][ii+3];
float (*bi)[ii+3]=new float[jj+kk+3][ii+3];
float (*bj)[ii+3]=new float[jj+kk+3][ii+3];

for (j=2;j<=jj+kk+1;j++)
    for (int i=1;i<=ii+2;i++)
        bi[j][i]=b[j][i]+aS[j][i]*T[j-1][i]+aN[j][i]*T[j+1][i];

float conv_crit=1; //initialization of the convergence criteria

// determination of the temperature by iterations in the x and the y direction by using the properties
// of tridiagonal matrices

```

```

while (conv_crit>pow(10,-4))
{
//sweep in the y_direction

for (j=2;j<=jj+kk+1;j++)
{
p[j][1]=aE[j][1]/a[j][1];
q[j][1]=b[j][1]/a[j][1];

for (i=2;i<=ii+2;i++)
{
p[j][i]=aE[j][i]/(a[j][i]-aW[j][i]*p[j][i-1]);
q[j][i]=(bi[j][i]+aW[j][i]*q[j][i-1])/(a[j][i]-aW[j][i]*p[j][i-1]);
}

T[j][ii+2]=q[j][ii+2];

for (i=ii+1;i>=1;i=i-1)
T[j][i]=p[j][i]*T[j][i+1]+q[j][i];

for (int u=2;u<=jj+kk+1;u++)
for (i=1;i<=ii+2;i++)
bi[u][i]=b[u][i]+aS[u][i]*T[u-1][i]+aN[u][i]*T[u+1][i];
}

for(j=1;j<=jj+kk+2;j++)
{ for(i=1;i<=ii+2;i++)
{ Ti[j][i]=T[j][i];}

//sweep in the x_direction

for (i=2;i<=ii+1;i++)
for(j=1;j<=jj+kk+2;j++)
bj[j][i]=b[j][i]+aW[j][i]*T[j][i-1]+aE[j][i]*T[j][i+1];

for (i=2;i<=ii+1;i++)
{
p[1][i]=aN[1][i]/a[1][i];
q[1][i]=b[1][i]/a[1][i];

for (j=2;j<=jj+kk+2;j++)
{

```

```

    p[j][i]=aN[j][i]/(a[j][i]-aS[j][i]*p[j-1][i]);
    q[j][i]=(bj[j][i]+aS[j][i]*q[j-1][i])/(a[j][i]-aS[j][i]*p[j-1][i]);

    }
    T[jj+kk+2][i]=q[jj+kk+2][i];

    for(j=jj+kk+1;j>=1;j=j-1)
        T[j][i]=p[j][i]*T[j+1][i]+q[j][i];

    for(j=1;j<=jj+kk+2;j++)
        for (int v=2;v<=ii+1;v++)
            bj[j][v]=b[j][v]+aW[j][v]*T[j][v-1]+aE[j][v]*T[j][v+1];
    }
    for(j=1;j<=jj+kk+2;j++)
        for(i=1;i<=ii+2;i++)
            Tj[j][i]=T[j][i];

conv_crit=convergence (Tj,Ti,jj); //compute the convergence value
}

Tj[jj+kk+2][1]=100;
Tj[jj+kk+2][ii+2]=100;

for(j=1;j<=jj+kk+2;j++)
    {
        for(i=1;i<=ii+2;i++)
            Point1_file<<Tj[j][i]<<" ";
            Point1_file<<"\n";
    }
for (i=1;i<=ii+2;i++)
    Point2_file<<x[i]<<"\n";// write the value of x in a file

for (j=1;j<=jj+kk+2;j++)
    Point3_file<<y[j]<<"\n";// write the value of y in a file

for (i=2;i<=ii+1;i++)
    total_heat+=k_bulk*dx[i]*2/dy[2]*(Tj[2][i]-Tj[1][i]);

//computation of ratio = k_eff/k_bulk

float ratio=total_heat*(H+ampl/2)/(L*k_bulk*(b[jj+kk+2][i]-b[1][i]));
Point4_file<<R/(R+H)<<" "<<ratio<<"\n"; // write the values of R/(R+H) and ratio in a file.
}
return 0;
}

```

Appendix D: heterog.cpp

 The program *heterog.cpp* is adapted from Vick and Scott [1998]. It computes the one-dimensional transient temperature distribution of the thermal radiation detector with doped thermal impedance, using the two-step process as developed in Section 4-1.

//Formulation

$$C_m \frac{T_{m,j}^i - T_{m,j}^{i-1}}{\Delta t} = K \frac{T_{m,j-1}^i - 2T_{m,j}^i + T_{m,j+1}^i}{(\Delta x)^2} - H(T_{m,j}^i - T_{p,j}^i) \quad (1)$$

$$C_p \frac{T_{p,j}^i - T_{p,j}^{i-1}}{\Delta t} = H(T_{m,j}^i - T_{p,j}^i) \quad (2)$$

//j control volume.

//T_{m,j} matrix temperature at the j location

//T_{p,j} particle temperature at the j location.

//The integration of the two equations above yields:

//From equation (2) we get

$$T_{p,j}^i = \frac{C_p}{C_p + H\Delta t} T_{p,j}^{i-1} + \frac{H\Delta t}{C_p + H\Delta t} T_{m,j}^i \quad (3)$$

//By replacing T_{p,j}ⁱ by (3) the equation (1) becomes:

$$\| a_j T_{m,j}^i - aW_j T_{m,j-1}^i - aE_j T_{m,j+1}^i = b_j \quad (4)$$

$$aO_{m,j} = \frac{C_m \Delta x}{\Delta t} \quad ; \quad aOp,j = \frac{HC_p \Delta x}{C_p + H\Delta t} \quad ; \quad aW_j = \frac{k_w}{\Delta x_w}$$

//

$$aE_j = \frac{k_E}{\Delta x_E} \quad ; \quad a_j = aO_{m,j} + aW_j + aE_j + aO_{p,j} \quad ; \quad b_j = aO_{m,j} * T_{m,j}^{i-1} + aO_{p,j} * T_{p,j}^{i-1}$$

//C++ headers

```
#include<math.h>
#include<iostream.h>
#include<fstream.h>
#include<stdio.h>
#define coef pow(10,-6)

//creation of data files

ofstream Point1_file("Matrix_temp.dat"); //matrix temperature file
ofstream Point2_file("Particles_temp.dat");// particles temperature file
ofstream Point3_file("y.dat"); //location
ofstream Point4_file("Temp_act_junct.dat"); //active junction temperature file

const int t_cvy=60;//total cv in the y_direction=sum of ny

//main program

int main()
{
//initialization

double density=0.01;//volume fraction of the particles
double dp=pow(10,-7);//diameter of the particles, m
double rocp=1860.2*pow(10,3);//heat capacity the particles
double vp=3.14*pow(dp,3)/6.0;//volume of a particle
double Np=density/vp;//number of particles in the thermal impedance layer per
volume;
double h=10; contact conductance, W/m^2.K
double Ap=3.14*dp*dp; //surface area of the particles, m^2
float Q=pow(10,6);//heat flux, W/m^2
double tmax=0.1;// time maxi, s
int n_time=100; // number of time steps
int count=1;
double dt=tmax/n_time;// time step, s
double t=0; //time
double kp=1.59;//thermal conductivity of the particles, W/m,K
double H[7]={0,coef,coef,25.4*coef,coef,coef,10*coef};//thickness of the layers
double conduct[7]={0,71.6,60,0.084,71.6,60,0.209};// layers conductivity
(W/m.K)
double ny[7]={0,10,10,10,10,10,10};//number of control volumes of each layer
double np[7]={0,0,0,Np,0,0,0};//number of particles
double Specific_heat[7]={0,133.0,200.0,712.0,133.0,200.0,669.0};//specific
heat (J/kg.K)
double Mass_density[7]={0,21450.0,6880.0,1289.0,21450.0,6880.0,1400.0};//Mass
density of the layers(kg/m^3)
```



```

int jj[7]={0};
double bio=h*dp/(6*kp); //computes the Biot number
double roc[7]={0}; //heat capacity of the layers
for (int i=1; i<=6; i++)
{
    roc[i]=Mass_density[i]*Specific_heat[i];
    jj[i]=jj[i-1]+ny[i];
}

double km[t_cvy+3]={0.0};
double Rocm[t_cvy+3]={0.0};
double K[t_cvy+3]={0.0};
double Cm[t_cvy+3]={0.0};
double Cp[t_cvy+3]={0.0};

int c=1;
for (int m=1; m<=6; m++)
{
    for (int j=c; j<=(jj[m]+2); j++) //effectives properties of the layers of the
        //thermal detector
        {
            km[j]=conduct[m];
            Rocm[j]=roc[m];
            K[j]=(1-np[m]*vp)*km[j];
            Cm[j]=(1-np[m]*vp)*Rocm[j];
            Cp[j]=np[m]*vp*roc[m];
        }
    c=jj[m]+2;
}

double dy[t_cvy+3]={0.0}; //step size vector, m
double y[t_cvy+3]={0.0}; //location vector, m

int d=2;
for(m=1; m<=6; m++)
{
    for (int j=d; j<=jj[m]+1; j++)
        dy[j]=H[m]/ny[m];
    d=jj[m]+2;
}

for (int j=2; j<=t_cvy+2; j++)
    y[j]=y[j-1]+0.5*(dy[j-1]+dy[j]);

for (j=1; j<=t_cvy+2; j++)
    Point3_file<<y[j]<<"\n";

//Initial temperature
double Tmprev[t_cvy+3]={0.0}; //matrix
double Tpprev[t_cvy+3]={0.0}; //particles;

Point4_file<<0<<" "<<0<<"\n"; //initial value of the active junction temperature.

double aN[t_cvy+3]={0.0};
double aS[t_cvy+3]={0.0};
double a[t_cvy+3]={0.0};
double b[t_cvy+3]={0.0};

```

```

double p[t_cvvy+3]={0.0};
double q[t_cvvy+3]={0.0};
double amO[t_cvvy+3]={0.0};
double apO[t_cvvy+3]={0.0};
double Tm[t_cvvy+3]={0.0};
double Tp[t_cvvy+3]={0.0};
-----
//Boundary conditions

// @ y=0          specified temperature, 0 K
aN[1]=0;
a[1]=1;
b[1]=0;

// @ y=H          specified heat flux Q
aS[t_cvvy+2]=2*km[t_cvvy+1]/dy[t_cvvy+1];
a[t_cvvy+2]=aS[t_cvvy+2];
b[t_cvvy+2]=Q;
-----

//Computation of the different coefficients aN,aS,amO,apOa,b

for(j=2;j<=t_cvvy+1;j++)
{
    aS[j]=2*K[j-1]*K[j]/(dy[j-1]*K[j]+dy[j]*K[j-1]);
    aN[j]=2*K[j]*K[j+1]/(dy[j]*K[j+1]+dy[j+1]*K[j]);
    amO[j]=Cm[j]*dy[j]/dt;
    apO[j]=Cp[j]*h*Np*Ap*dy[j]/(Cp[j]+h*Np*Ap*dt);
    a[j]=amO[j]+apO[j]+aS[j]+aN[j];
}
-----

//computation of the matrix and particle temperature by solving the coupled
//Equations 3 and 4. Equation 4 is solved by using the tridiagonal matrix
properties.

for (count=1;count<=n_time;count++)
{
t+=dt;

    for(j=2;j<=t_cvvy+1;j++)
        b[j]=amO[j]*Tmprev[j]+apO[j]*Tpprev[j];

    p[1]=aN[1]/a[1];
    q[1]=b[1]/a[1];

    for (j=2;j<=t_cvvy+2;j++)
    {
        p[j]=aN[j]/(a[j]-aS[j]*p[j-1]);
        q[j]=(b[j]+aS[j]*q[j-1])/(a[j]-aS[j]*p[j-1]);
    }

    Tm[t_cvvy+2]=q[t_cvvy+2];

    for(j=t_cvvy+1;j>=1;j=j-1)
        Tm[j]=p[j]*Tm[j+1]+q[j];
}

```

```

for (j=1;j<=t_cvx+2;j++)
{
    Tmprev[j]=Tm[j];
    Point1_file<<t*pow(10,3)<<" "<<Tm[j]<<"\n";
}
//write the temperature of the active junction in a file
Point4_file<<t*pow(10,3)<<" "<<Tm[jj[4]+1]<<"\n";

for (j=jj[2]+2;j<=jj[3]+1;j++)
{
    Tp[j]=(h*Np*Ap*dt*Tm[j]+Cp[j]*Tpprev[j])/(Cp[j]+h*Np*Ap*dt);
    //write the temperature of the particles in a file
    Point2_file<<t<<" "<<Tp[j]<<"\n";
}

Point5_file<<t*pow(10,3)<<" "<<Tm[jj[2]+4]<<" "<<Tp[jj[2]+4]<<"\n";

for (j=1;j<=t_cvx+2;j++)
    Tpprev[j]=Tp[j];

}

return 0;
}

```

Vita

Mamadou Yaya Barry was born on [REDACTED], [REDACTED], in [REDACTED] in the [REDACTED] [REDACTED]. He grew up and studied in different cities (Kindia, Coyah, Boffa, Kissidougou). For his first six years at school he studied in “soussou”, one the many languages in Guinea!!! After he obtained his high school diploma (bac) he spent two years studying Electrical Engineering at the *Institut Polytechnique de Conakry*.

In 1993 he traveled to France and prepared a *Diplôme Universitaire de Technologie* in Chemical Engineering at the *Institut Universitaire de Nancy Brabois*. After his graduation he enrolled at the *Université de Technologie de Compiègne* (UTC) to prepare a *Diplôme d'ingénieur* in Chemical Engineering. During his last semester at the UTC he was accepted at Virginia Polytechnic Institute and State University for a Master of Science in Mechanical Engineering. At Virginia Tech he served as a graduate research assistant in the Thermal Radiation Group. He received his *Diplôme d'ingénieur* in Chemical Engineering in October 1999 and his Master of Science in Mechanical Engineering in December 1999. He plans to work at least one year in the United States in order to gain more engineering experience.

Mamadou Y. Barry